

## ABSTRACT

RILEY, Tiffany Lynn. Nanocrystalline Metal/Metal Hydrides for Fuel Cell Applications.

(Under the direction of Jagannadham Kasichainula.)

Formation of nanocrystalline films by low temperature deposition of metallic films was investigated with special emphasis for hydrogen storage. Large grain boundary volume associated with nanocrystalline films was shown to be favorable for hydrogen absorption and hydride formation in zirconium and titanium metals.

Nanocrystalline films of titanium and zirconium were deposited on porous alumina and silicon substrates via low temperature deposition ( $-50^{\circ}\text{C}$ ). Low substrate temperature was obtained by circulating nitrogen gas through the substrate holder. Nitrogen gas was cooled by passing through a coil that was submerged in liquid nitrogen. The films were charged with hydrogen via molecular and ionic charging. The films were characterized for microstructure, crystallinity, hydrogen capacity, and kinetics of hydrogen absorption and desorption using several techniques including transmission electron microscopy (TEM), X-ray diffraction (XRD), scanning electron microscopy (SEM), optical microscopy, secondary ion mass spectrometry (SIMS), and electrical resistance measurements. High resolution TEM was used to determine the volume fraction of amorphous region and grain size. The shift in the X-ray diffraction peaks with lattice parameter changes resulting from hydrogen incorporation in the lattice and the increase in half-peak-width with smaller grain size were determined. X-ray mapping, line scan, and energy dispersive spectrometry (EDS) to identify different elements present in the films

were used along with secondary electron imaging in the SEM to determine morphology and composition. Optical microscopy was also employed at higher magnification to examine the morphology of the hydrides from the surface of the films. The relative hydrogen capacity in the hydrogen charged films compared to that in the films without hydrogen charging was determined by SIMS depth profiling analysis. Electrical resistance measurements as a function of temperature were instrumental in identifying the presence of hydrogen in the films. Annealing with varying temperature was carried out to determine the kinetics of desorption.

The results show that the films deposited at low temperature were much smaller in grain size than those deposited at room temperature. Hydrogen concentration was much greater in the films deposited at low temperature, and also, hydride concentration was much higher in the hydrogen plasma treated (ionic charged) films deposited at low temperature. The results clearly show that low temperature physical vapor deposition of nanocrystalline films is a favorable method for zirconium and titanium alloys.

# **NANOCRYSTALLINE METAL/METAL HYDRIDES FOR FUEL CELL APPLICATIONS**

by

**TIFFANY L. RILEY**

A thesis submitted to the Graduate Faculty of  
North Carolina State University  
in partial fulfillment of the  
requirements for the Degree of  
Master of Science

**MATERIALS SCIENCE AND ENGINEERING**

Raleigh

2005

**APPROVED BY**

\_\_\_\_\_  
John Bartley

\_\_\_\_\_  
J. M. Rigsbee

\_\_\_\_\_  
Jag Kasichainula  
Chair of Advisory Committee

## **DEDICATION**

I dedicate this work to Dr. Jag Kasichainula, who has been my advisor, mentor, and friend throughout my graduate experience. It was his dedication, passion, willingness to help, and words of encouragement that drove me through my graduate research.

## **BIOGRAPHY**

TIFFANY L. RILEY was born in East Liverpool, Ohio on November 6<sup>th</sup>, 1980. In 1987, she moved to Concord, NC where she remained until 1999 when she graduated with honors from Central Cabarrus High School. In the fall of 1999, Tiffany began her college career at North Carolina State University (NCSU) in Textile Engineering supported by the College of Textiles Spectrum Dyed Yarns Merit Scholarship. In the spring of 2003, Tiffany received a Bachelor of Science degree in Textile Engineering from NCSU, while graduating Summa Cum Laude. In addition to graduating Summa Cum Laude, she was a member of the National Society of Collegiate Scholars, and she successfully completed the NCSU Scholar's program. Upon graduation, Tiffany worked for Milliken and Company as a Product and Process Improvement Engineer. In the spring of 2004, she left Milliken and Company to continue her education at NCSU by pursuing a Master of Science degree in Materials Science and Engineering, while working toward a minor in Business Management – Entrepreneurship.

## ACKNOWLEDGEMENTS

I would like to thank my advisor, Dr. Jag Kasichainula, for all of his guidance and support to perform this research. I take this opportunity to thank Dr. Mike Rigsbee and Dr. Jon Bartley for being committee members, as well as for their guidance. My special thanks go to Dr. Tom Watkins and Dr. Larry Allard Jr. from High Temperature Materials Laboratory at Oak Ridge National Laboratory for continuous help and encouragement during and after the summer research program, Mr. Fred Stevie, and Mr. Chad Parish from Analytical Instrumentation Facility for their special assistance and help with characterization techniques. I thank Dr. Lew Reynolds for continuous support and guidance during my teaching assistantship. I thank all members of the Department of Materials Science and Engineering including Mr. Roger Russell, Mr. Dan Leonard, Mr. Chris McGinnis, Ms. Edna Deas, Ms. Deip Vo, Mr. Marcus Hunt, Dr. Meredith Reed, and Dr. Mason Reed for enjoyable interaction, and Dr. Andrew Payzant from High Temperature Materials Laboratory and Prof. Tom Hutchinson of South Eastern Universities Research Association for their help in the summer research. My special appreciation goes to the Materials Science and Engineering Department for providing me with teaching assistantships to fund my way through the graduate program. This research is supported partially through SURA-ORNL summer research program, Oak Ridge National Laboratory, and National Science Foundation. I am very grateful to my family and friends for their support throughout my graduate program.

# TABLE OF CONTENTS

<b>LIST OF TABLES .....</b>	<b>vii</b>
<b>LIST OF FIGURES .....</b>	<b>viii</b>
<b>1. INTRODUCTION.....</b>	<b>1</b>
1.1. Technical Support .....	1
1.2. Hydrogen Storage Mediums and Techniques .....	2
1.3. Physical and Chemical Properties of Metal Hydrides .....	3
1.3.1. Advantages of Nanostructured Materials.....	5
1.4. Kinetics of Hydrogen Sorption .....	6
1.5. Synthesis .....	10
1.6. Fuel Cells and the Hydrogen Economy .....	11
1.7. Motivation.....	12
1.8. Thesis Overview .....	13
<b>2. EXPERIMENTAL.....</b>	<b>17</b>
2.1. Materials and Sample Preparation .....	17
2.2. Physical Vapor Deposition .....	18
2.2.1. Room Temperature Deposition.....	20
2.2.2. Lower Temperature Deposition .....	20
2.3. Hydrogen Charging.....	22
2.4. X-ray Diffraction .....	23
2.5. Resistance Measurements .....	25
2.6. Microscopy .....	28
2.6.1. Optical Microscopy.....	28
2.6.2. Scanning Electron Microscopy .....	28
2.6.3. Transmission Electron Microscopy .....	29
2.7. Secondary Ion Mass Spectrometry .....	30
2.8. Kinetics of Absorption and Desorption .....	31
<b>3. MORPHOLOGY OF NANOCRYSTALLINE FILMS .....</b>	<b>33</b>
3.1. Scanning Electron Microscopy .....	33
<b>4. GRAIN SIZE DETERMINATION.....</b>	<b>34</b>
4.1. X-ray Diffraction .....	34
4.2. Transmission Electron Microscopy .....	41
4.2.1. High Resolution TEM.....	41
4.2.2. TEM Diffraction Patterns .....	44
<b>5. IDENTIFICATION OF ELEMENTS AND OBSERVATION OF HYDRIDES</b>	
.....	<b>46</b>
5.1. X-ray Diffraction .....	46
5.2. Optical Microscopy.....	49
5.3. Scanning Electron Microscopy.....	50

5.4.	Resistance Measurements .....	54
5.5.	Secondary Ion Mass Spectrometry .....	56
<b>6.</b>	<b>KINETICS OF ABSORPTION AND DESORPTION .....</b>	<b>65</b>
6.1.	Pressure Versus Temperature Measurements .....	65
<b>7.</b>	<b>MODELING .....</b>	<b>69</b>
7.1.	Volume Fraction of Amorphous Grain Boundary Region.....	69
7.1.1.	Cubic System .....	69
7.1.2.	3-D Hexagonal System .....	71
<b>8.</b>	<b>CONCLUSIONS AND FUTURE WORK .....</b>	<b>76</b>
<b>9.</b>	<b>BIBLIOGRAPHY .....</b>	<b>80</b>

## LIST OF TABLES

TABLE 1.1. Key Properties of Metal Hydrides Suitable for Gas-Phase Applications. ....	4
TABLE 4.1. Table of FWHM and XS Comparisons for Samples of Nanocrystalline Zr Films on Si Substrates with Corrected FWHM Values.. .....	36
TABLE 4.2. Table of FWHM and XS Comparisons for Samples of Nanocrystalline Zr Films on Al <sub>2</sub> O <sub>3</sub> Substrates with Corrected FWHM Values.. .....	38
TABLE 4.3. Table of FWHM and XS Comparisons for Samples of Nanocrystalline Ti Films on Si Substrates.. .....	39
TABLE 4.4. Table of FWHM and XS Comparisons for Samples of Nanocrystalline Ti Films on Al <sub>2</sub> O <sub>3</sub> Substrates. ....	40

## LIST OF FIGURES

FIGURE 2.1. Porous alumina substrate taped to silicon. ....	17
FIGURE 2.2. Magnetron sputtering unit. ....	18
FIGURE 2.3. Cooling apparatus for lower temperature deposition. ....	21
FIGURE 2.4. Low temperature dewar for resistivity measurements.....	27
FIGURE 2.5. Diagram of SIMS operation. ....	31
FIGURE 3.1. SEM images of room temperature deposited Ti film (a) and lower temperature deposited Zr film (b) on Al <sub>2</sub> O <sub>3</sub> substrates, showing sample morphology.....	33
FIGURE 4.1. XRD Graph of Zr (103 reflection), showing peak broadening. ....	34
FIGURE 4.2. HRTEM image showing nanocrystalline grain sizes in the room temperature (a) and the lower temperature (b) deposited Ti films. ....	41
FIGURE 4.3. HRTEM image showing nanocrystalline grain sizes in the room temperature (a) and lower temperature (b) deposited Zr films. ....	42
FIGURE 4.4. HRTEM image showing nanocrystalline grain sizes in the room temperature (a) and lower temperature (b) deposited Zr films that were heat treated to 573 K.....	43
FIGURE 4.5. TEM diffraction patterns of the room temperature deposited Ti film (a) and the lower temperature deposited Ti film (b). ....	45
FIGURE 4.6. TEM diffraction patterns of the room temperature deposited Zr film (a) and the lower temperature deposited Zr film (b). ....	45
FIGURE 5.1. XRD graph of Intensity vs. 2 Theta of Zr films on Si substrates: RT PH – room temperature deposited film with hydrogen plasma treatment; LT PH – low temperature deposited film with hydrogen plasma treatment; LT no H – low temperature deposited film with no hydrogen treatment .....	46
FIGURE 5.2. XRD graph of Intensity vs. 2 Theta of Zr films on Al <sub>2</sub> O <sub>3</sub> substrates: RT no H – room temperature deposited film with no hydrogen treatment; RT MH – room temperature deposited film with molecular hydrogen treatment; LT no H – low temperature deposited film with no hydrogen treatment; LT MH – low temperature deposited film with molecular hydrogen treatment. ....	47
FIGURE 5.3. XRD graph of Intensity vs. 2 Theta of Ti films on Si substrates: RT no H – room temperature deposited film with no hydrogen treatment; RT PH – room temperature deposited film with hydrogen plasma treatment; LT PH – low temperature deposited film	

with hydrogen plasma treatment; LT no H – low temperature deposited film with no hydrogen treatment. ....	48
FIGURE 5.4. XRD graph of Intensity vs. 2 Theta of Ti films on Al <sub>2</sub> O <sub>3</sub> substrates: RT no H – room temperature deposited film with no hydrogen treatment; RT MH – room temperature deposited film with molecular hydrogen treatment; LT no H – low temperature deposited film with no hydrogen treatment; LT MH – low temperature deposited film with molecular hydrogen treatment. ....	49
FIGURE 5.5. Optical micrographs of both the room temperature (a) and the lower temperature (b) deposited Zr films on Si substrates that underwent hydrogen plasma treatment, showing presence of hydrides.....	50
FIGURE 5.6. SEM (backscattered mode) EDS spectrums of the room temperature deposited Ti film on porous Al <sub>2</sub> O <sub>3</sub> substrate (a) and the lower temperature deposited Zr film on porous Al <sub>2</sub> O <sub>3</sub> substrate(b), verifying presence of titanium and zirconium. ....	51
FIGURE 5.7. SEM (secondary electron mode) image of the lower temperature deposited Zr film on a Si substrate that underwent hydrogen plasma treatment, showing presence of hydrides.....	52
FIGURE 5.8. SEM map and line scan of the lower temperature deposited Zr film on a Si substrate that underwent hydrogen plasma treatment. Starting from the top and going right to left, the k-alpha signal from carbon is 70, oxygen – 575, background – 96, silicon – 742, and zirconium – 2084.....	53
FIGURE 5.9. Graph of resistance (Ohm) vs. temperature (K) of Zr films on Si substrates: Zr-LT-H – low temperature deposited film with molecular hydrogen treatment; Zr-RT-H – room temperature deposited film with molecular hydrogen treatment; Zr-RT – room temperature deposited film with no hydrogen treatment; Zr-LT – low temperature deposited film with no hydrogen treatment. ....	55
FIGURE 5.10. Graph of resistance (Ohm) vs. temperature (K) of Ti films on Si substrates: Ti-RT-H – room temperature deposited film with molecular hydrogen treatment; Ti-RT – room temperature deposited film with no hydrogen treatment. ....	56
FIGURE 5.11. SIMS (secondary ion mass spectrometry) graph of counts/sec vs. depth of hydrogen content in Zr films on Si substrates: LT HP 4 – low temperature deposited film with hydrogen plasma treatment; RT HP 5 – room temperature deposited film with hydrogen plasma treatment; LT no H 6 – low temperature deposited film with no hydrogen treatment. ....	57
FIGURE 5.12. SIMS (secondary ion mass spectrometry) graph of counts/sec vs. depth of oxygen content in Zr films on Si substrates: LT HP 4 – low temperature deposited film with hydrogen plasma treatment; RT HP 5 – room temperature deposited film with hydrogen plasma treatment; LT no H 6 – low temperature deposited film with no hydrogen treatment. ....	59

FIGURE 5.13. SIMS graph of counts/sec vs. depth of a hydrogen standard for measuring elements 1H, 28Si, and 90Zr. The standard was provided by NCSU SIMS specialist, Fred Stevie. ....	60
FIGURE 5.14. SIMS graph of counts/sec vs. depth of a low temperature deposited Zr film on Si substrate with no hydrogen treatment. Measurements were taken to determine presence of elements 1H, 28Si, and 90Zr. ....	61
FIGURE 5.15. SIMS graph of counts/sec vs. depth of a low temperature deposited Zr film on Si substrate with hydrogen plasma treatment. Measurements were taken to determine presence of elements 1H, 16O, 28Si, and 90Zr. ....	62
FIGURE 5.16. SIMS graph of counts/sec vs. depth of a room temperature deposited Zr film on Si substrate with hydrogen plasma treatment. Measurements were taken to determine presence of elements 1H, 16O, 28Si, and 90Zr. ....	63
FIGURE 6.1. Generic graph of pressure versus temperature to illustrate parameter relationship. ....	65
FIGURE 6.2. Pressure vs. Temperature graph of nanocrystalline zirconium samples on silicon substrates with different deposition temperatures and hydrogen treatments. ....	67
FIGURE 7.1. Cubic system basis for amorphous volume fraction calculations. ....	69
FIGURE 7.2. 3-D hexagonal system basis for amorphous volume fraction calculations. ....	71
FIGURE 7.3. Hexagonal surface for area calculation. ....	71
FIGURE 7.4. Equal diameter grains with varying 'd' dimensions between the cubic and hexagonal shapes. ....	73
FIGURE 7.5. Illustration for determining the average amorphous region per grain. ....	74
FIGURE 7.6. Graph illustrating the effect of grain size as well as grain shape on the amorphous volume fraction of a system. ....	75

# NANOCRYSTALLINE METAL/METAL HYDRIDES FOR FUEL CELL APPLICATIONS

## 1. INTRODUCTION

### 1.1. Technical Support

Hydrogen is envisaged to be of great importance for future energy applications, in particular, as an alternative fuel for both combustion engines and fuel cells [1]. It provides clean fuel that is environmentally very safe and friendly. Because hydrogen storage in liquid or gaseous forms imposes safety problems, metal hydrides offer a safe storage alternative and also have a higher volumetric density.  $MgH_2$  has the highest storage capacity (9.1wt% H [2]) but microcrystalline  $MgH_2$  exhibits low desorption kinetics at 300 K. Light metal hydrides are more advantageous, however, they exhibit sluggish absorption kinetics [2,3]. Nanocrystalline light metal hydrides have shown [4] very fast absorption kinetics and therefore offer new opportunities. Intensive mechanical milling has been used to make nanocomposites of magnesium hydride and transition metals such as Ti, V, Mn, Fe and Ni that act as catalysts [5] by increasing the reaction kinetics with decreased desorption and increased absorption temperatures. Similarly, nanocomposites of Mg hydrides with metal oxides were found to be good candidates with good absorption properties because of the catalytic action of the oxides [6]. In particular, the catalytic effects of  $TiO_2$ ,  $V_2O_5$ ,  $Cr_2O_3$ ,  $Mn_2O_3$ ,  $Fe_3O_4$  and  $CuO$  in both desorption and absorption was noted [7].

## **1.2. Hydrogen Storage Mediums and Techniques**

There are primarily three forms of hydrogen storage: gaseous, liquid, and solid-state forms. Gaseous storage of hydrogen, as compressed hydrogen gas is the oldest method. The major disadvantages of gaseous hydrogen for automotive and fuel cell applications are its low volumetric density and its safety concern as a highly flammable gas. One kilogram of hydrogen stored in common gas cylinders at 2,200 psi occupies 91.2 liters, with an effective energy density of 1.6 MJ/L, which is equivalent to the energy carried by 8.2 L of gasoline [8]. Even at 10,000 psi pressures, the energy content is considerably less than that for the same volume of gasoline – 4.4 MJ/L for hydrogen compared with 31.6 MJ/L for gasoline [9]. Therefore, gaseous storage of hydrogen is not the most preferred form when being considered for fuel cell applications.

While liquid hydrogen has a much larger effective energy density, 8.4 MJ/L, than that of gaseous hydrogen with 4.4 MJ/L, it still does not meet the required values for the FreedomCar. Other drawbacks of liquid hydrogen are the safety hazard posed through “boil-off” of hydrogen, loss of hydrogen due to evaporation, and the very large amount of energy that is required for liquefaction. These drawbacks make liquid hydrogen a non-promising method of storing hydrogen for automotive and fuel cell applications.

As opposed to gaseous and liquid hydrogen, solid state storage in the form of metal hydrides offers a promising method of hydrogen storage, as a subset of hydrides can nominally meet volumetric and gravimetric density (9 wt. %) requirements [10]. While

this is a promising concept, there are many obstacles that need to be overcome before these metal hydrides will be useable for hydrogen fuel cells. Metal hydrides have such a high gravimetric density because of the ionic or covalent bonding of hydrogen to the metal sublattice. As a result of these strong bonds, the desorption of hydrogen requires temperatures that are well above the desired range of  $-20^{\circ}\text{C}$  to  $100^{\circ}\text{C}$  and pressures above the desired range of 1-10 bar [10]. Understanding the physics and chemistry behind hydrogen absorption and desorption in metal hydrides is a critical factor for real development of usable forms of hydrides.

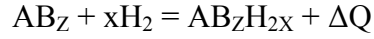
### **1.3. Physical and Chemical Properties of Metal Hydrides**

As a gas, hydrogen exists in the form of molecular  $\text{H}_2$ , which liquefies at 12K and solidifies at 4K. Under high pressure, it should transform into an atomic solid, the simplest metal, and possibly a room-temperature superconductor [11]. Hydrogen is the best element in terms of its electron to nucleon ratio, which characterizes it with very high energy per mass, thus making it an ideal energy source.

Intermetallic compounds for metal hydrides of types A, AB,  $\text{AB}_2$ ,  $\text{AB}_5$ ,  $\text{A}_2\text{B}$ , and body-centered cubic metals are well characterized with well-known values for interstitial hydrogen storage ranging between 1.4 and 3.6 wt% hydrogen [9]. Some examples of these compounds are TiFe,  $\text{ZrMn}_2$ ,  $\text{LaNi}_5$ , and MgNi. Of these examples, the MgNi alloy is the most promising in terms of ability to store the largest amount of hydrogen, as Mg alloys have proven to store the maximum amount of hydrogen by weight percent over

other alloys of rare-earth or transition metals. Alloys of Mg have shown hydrogen capacities in the range of 3.3-7.7 wt% [12].

The desired reaction for a generic intermetallic alloy  $AB_Z$  with hydrogen gas is:



where  $\Delta Q$  is the heat released upon absorption of hydrogen. Typically in these alloys, the A metal, or ideally Mg, forms stable binary hydrides, while the B metal is that which may aid in dissociation of hydrogen. Table I represents a list of possible hydrides from the five metal hydrides mentioned earlier that have shown the most promise for practical hydrogen storage [12].

TABLE 1.1. Key Properties of Metal Hydrides Suitable for Gas-Phase Applications [12].

Alloy Type	Hydride Phase	Maximum H Capacity (wt%)	Reversible H Capacity (wt%)	$P_{des}$ at 298 K (bar)	T(K) for $P_{des} = 1.013$ bar
A	MgH <sub>2</sub>	7.66	< 7.0	$\sim 10^{-6}$	552
A	VH <sub>2</sub>	3.81	1.9	2.1	285
A <sub>2</sub> B	Mg <sub>2</sub> NiH <sub>4</sub>	3.59	3.3	$\sim 10^{-5}$	528
AB	TiFeH <sub>2</sub>	1.89	1.5	4.1	265
AB	ZrNiH <sub>3</sub>	1.96	1.1	$\sim 5 \times 10^{-6}$	573
AB <sub>2</sub>	TiMn <sub>1.4</sub> V <sub>0.62</sub> H <sub>3.4</sub>	2.15	1.1	3.6	268
AB <sub>2</sub>	ZrMn <sub>2</sub> H <sub>3.6</sub>	1.77	0.9	0.001	440
AB <sub>5</sub>	LaNi <sub>5</sub> H <sub>6.5</sub>	1.49	1.28	1.8	285
AB <sub>5</sub>	LaNi <sub>4.8</sub> Sn <sub>0.2</sub> H <sub>6.0</sub>	1.40	1.24	0.5	312

From this table, it is evident that Mg offers the highest maximum hydrogen capacity by far at 7.66 wt%, but on another note, it also requires one of the highest temperatures for desorption at 1.013 bar pressure.

### ***1.3.1. Advantages of Nanostructured Materials***

More recent research on nano-scaled materials has shown promising results with respect to hydrogen storage capacity, sorption properties, and kinetics. The small size of nanostructured materials strongly influences the thermodynamics and kinetics of hydrogen adsorption and dissociation by increasing the diffusion rate, as well as by decreasing the required diffusion length [9]. Nano-scale materials may increase diffusion rates by means of increased amorphous area containing more sites for hydrogen to enter the material.

There are two main categories of nano-scale hydrogen storage materials: atomic and molecular. Atomic hydrogen storage materials involve bonding of hydrogen atoms with the storage medium lattice, which requires reversible dissociation of molecular hydrogen into the hydrogen atoms. Molecular hydrogen storage materials containing high surface area and microporosity store hydrogen by means of weak molecular surface interactions, such as van der Waals forces [9].

Amorphous structures produced by nonequilibrium techniques are widely varying and a wide distribution of hydrogen absorbing sites are present [12]. Although both crystalline and amorphous structures have the same composition, both exhibit a widely differing hydrogenation behavior. The constant pressure region (plateau) in a range of composition of hydride is not observed in the amorphous phases. Similarly, the fraction of amorphous phase present in nanocrystalline microstructure plays an important role in the

hydrogenation behavior of hydrides. The large volume fraction of amorphous region present along grain boundaries in nanocrystalline microstructures offers many atomic sites for hydrogen occupation and as a result enhanced solubility is expected in nanocrystalline structures with smaller grain size. In the presence of higher solubility in the amorphous enclave around the nanocrystalline grains, higher hydrogen solubility also exists within the grains [12]. Our proposed synthesis by PVD allows ultimate solubility to be reached within the amorphous and crystalline regions because ionic hydrogen can diffuse very fast along the grain boundaries. The degree of amorphization present in the nanocrystalline microstructure defined as the ratio of amorphous regions along grain boundaries to crystalline region in the lattice increases with decreasing grain size and it will be an important microstructural parameter to be controlled. It is very important that the volume fraction of the grain boundary amorphous enclave is increased or the grain size reduced without disturbing the composition.

#### **1.4. Kinetics of Hydrogen Sorption**

The rate of absorption of hydrogen is limited by:

1. Rate of hydrogen dissociation at the surface.
2. Diffusion through the barrier layer such as an oxide on the surface.
3. Diffusion of hydrogen through the crystalline or amorphous region.
4. Diffusion through any hydride layer present on the surface.

Development of new materials with improved hydrogen concentration requires new processing techniques that can eliminate some of the above steps. Overcoming the diffusion barriers and improving the diffusion rate by provision of catalyst phases that eliminate the need for hydrogen activation are some of the advantages. It has been shown that hydrogen diffusion in nanocrystalline palladium is faster compared to that in single crystal palladium [13]. Hydrogen diffusion begins with filling of easily accessible sites at the disordered grain boundary regions and thereby access to the nanocrystalline regions becomes easier. Large surface to volume ratio improves the hydrogen absorption. Significant improvements have been found in the absorption of hydrogen in nanocrystalline phases compared to the single crystal region [12].

Other factors can improve the absorption radically when kinetic limitations can be removed. Hydrogen dissociation is one of the critical factors in the hydrogen absorption. Oxides on metal surfaces actually help dissociation of hydrogen molecules but defeat the action by becoming a barrier to diffusion. Catalysts enable fast and effective dissociation and also improve uniform distribution provided there is no interfacial layer of oxide. In mechanical alloying by ball milling, this may still be one of the hurdles to overcome. On the other hand, a catalyst can be co-deposited along with the hydride-forming phase in a reactive hydrogen environment in vapor deposition of nanocrystalline phases. The efficiency of the catalyst depends on how well it can flood the hydride-forming phase with atomic hydrogen. Several investigations have shown that perfect oxide single crystal surfaces are inert towards reaction with  $H_2$ . However,  $H_2$  is absorbed by  $TiO_2$  surfaces with high density of defects

such as present across the interface between metal and oxide [6]. A very small amount of palladium (less than 1%) in nanocrystalline form can provide atomic hydrogen for the hydride-forming phase. The presence of catalyst makes the hydride-forming phase insensitive to presence of oxides. Vapor deposition process can completely avoid oxide formation by good vacuum prior to deposition. The kinetics of desorption follows the same principles namely hydrogen should diffuse and recombine on the surface.

Ball milled  $\text{MgH}_2$  without any catalyst can not desorb hydrogen at 523 K while  $\text{MgH}_2$  with 5 at%Ti or 5 at% V composites can desorb hydrogen at 523 K within 1000 seconds [5]. At lower temperatures than 523 K,  $\text{MgH}_2$  with vanadium shows the best desorption kinetics. The rate of desorption has been found to be limited by the metal/hydride interface movement or the diffusion controlled process. The activation energy for hydrogen desorption ( $\sim 60$  KJ/mol) has been found to be much lower than its value in the pure  $\text{MgH}_2$  ( $\sim 120$  kJ/mol). While vanadium is most suited for desorption, titanium is effective in improving the absorption kinetics in the range of 300 to 475 K. All transition elements (Ti, V, Fe, Mn, and Ni) are effective in improving the absorption.  $\text{MgH}_2$  with Ni is better than Mg-Ni alloy that was ball milled. Nickel is not as good a catalyst as Ti and V. However, oxide formation is inevitable in ball milled nanocrystalline alloys and in particular Ti and V are very sensitive to stable oxide formation. Nickel oxide can easily be reduced in the presence of hydrogen. Any oxygen released by reduction process may oxidize and form MgO that is also stable. Thus, it appears that one of the disadvantages of ball milling process is the tendency for oxide formation during reduction of grain size to nanoscale.

Even when milled in the presence of hydrogen, prevention of oxide formation with lower free energy of formation than that of the hydride is not thermodynamically favorable. Oxides also are catalysts in the hydrogen sorption processes, however, only when present as nanodispersions.

Noticeable enhancement of both absorption and desorption kinetics has been observed in alloys obtained by simultaneous milling of hydride and oxide phases. Among the best oxides,  $\text{Fe}_3\text{O}_4$  and  $\text{V}_2\text{O}_5$  are the most effective in desorption whereas  $\text{Cr}_2\text{O}_3$  yields the highest absorption kinetics. The catalyst content need not be very high and can be as low as 0.3 vol % or 1 wt%. Certain elements like Ti and V form a hydride by themselves and help to supply hydrogen as a catalyst whereas certain other elements like Mn and Ni are not hydride forming. The transition metal catalysts chemisorb hydrogen and transfer it to Mg or its alloy. The interface between the catalyst and the Mg alloy acts as a nucleation site for the hydride phase and thus reduces the nucleation barrier. Similarly, the rate limitation step for desorption is metal/hydride interface boundary migration and does not seem to involve nucleation and growth of metal in hydride. Also, structural defects formed at the interface seem to be very effective in the nucleation process of hydrides. Before hydrogen can be absorbed, it should be adsorbed at the surface and adsorption is effective at dangling bonds that will be occupied by hydrogen. Mechanical milling could be effective in creating the defects. Thus, it appears that Ti, V, Cr, and Fe are the best candidates for catalyst use in Mg alloys while Pd could also be very effective non-transition element for hydride formation. Hysteresis is of considerable practical importance since it reduces the efficiency of hydrogen

storage system. In particular, the strain energy associated with occupation of interstitial sites by hydrogen or defect sites where hydrogen binding is high could be responsible for the occurrence of hysteresis [14]. A better understanding of the mechanisms will help to minimize hysteresis.

## **1.5. Synthesis**

Conventional hydrogen storage materials are made in the cast form. However, the more recent technique of mechanical alloying with ball milling has gained considerable importance in making the hydrides. The drastic improvement of hydrogen absorption and desorption properties is caused by milling process, thus, reducing the grain size to nanocrystalline range [2]. Mechanical alloying is performed in conventional ball milling with additional hydrogen atmosphere maintained at the desired level. The low cost and ease of formation of composites of one or more elements is a definite advantage. However, contamination from ball milling apparatus is one disadvantage. Oxide formation even in the presence of hydrogen atmosphere has been observed because of the poor vacuum to start with. Oxide formation, as mentioned previously, could be both advantageous and disadvantageous in hydride synthesis and to improve the kinetics of absorption and desorption because on one hand oxides act as catalyst and on the other as barrier layer. In addition, the specific surface area of these materials made by ball milling is usually less than 1 sq.meter/gm due to cold welding of particles during milling. It has been suggested that ball milling metal hydrides rather than the metal in the presence of hydrogen improves the hydrogen sorption kinetics [2,6]. The defect structure produced at the interfaces and the

internal defect structure produced in the hydrides is considered more favorable for hydrogen absorption [5]. Further more, in certain alloys such as Zr-Cr-Ni hydrides, mechanical alloying by ball milling is not effective in producing nanocrystalline C14 structures and further heat treatment was needed [15].

More recently combustion synthesis (SHS) has been used for formation of Ti(Zr) hydrides. Such a process is favorable because the hydride reactions are exothermic. Complex hydride-nitrides are also produced in a two-stage synthesis, first partial nitridation followed by hydride formation. The temperatures of formation are high (820°C for TiH<sub>2</sub>) and the volume changes are severe. The process also leads to porous nanocrystalline structure, a real advantage. Also, hydride formation is not complete since the hydrogen diffusion must occur into the nanograins through the outer hydride layer that is already formed first. Nanocrystalline phases made by gas phase condensation in the presence of hydrogen atmosphere are free from these disadvantages [16,17]. In addition, hydrogen absorption in the gas phase is much improved requiring no activation. The surface areas of the nanocrystalline composites can be increased 40 to 50 times to that obtained by mechanical alloying.

## **1.6. Fuel Cells and the Hydrogen Economy**

Fuel cells, which operate by the transformation of chemical energy from hydrogen fuel into electrical energy, have been a major focus in the development of a hydrogen economy. They are an ideal source of energy for many applications such as power

plants, automobiles, cell phones, and personal computers because they operate with high efficiency and they do not cause pollution [9,12] Many efforts are being made to make hydrogen fuel a reality.

## **1.7. Motivation**

There are many valuable opportunities relating to the development and management of energy sources that are friendly to the environment, which is very much what our country needs. I have been performing research on hydrogen storage materials, in particular, nanocrystalline materials that have been shown to exhibit high hydrogen solubility. The purpose of my research is to store hydrogen that can be used for several applications, including nuclear fusion, fuel cell applications, and advanced heat engine applications. Foremost of these are fuel cell applications which offer a promising alternative energy source for major applications such as power plants and automobiles.

Fuel cells are of great importance as they are sources of clean, pollution-free energy. Not to mention, hydrogen is the most abundant element in the universe, as it is available in small quantities in air and in unlimited amounts, though chemically bound, in water. Along the lines of pollution-free energy, thermal power that is currently being used has been found not to be dependable as overloaded power transmission lines and failure of power plants lead to black outs and lack of power. As research indicates, the pollution levels in the areas of the black out declined soon after the black out, thus illustrating the source of pollution in the North Eastern States of the United States. In addition to this,

hydrogen is a rich source of energy that has been discovered long before gasoline operated vehicles came into existence, and it is not too late to develop and equip ourselves with this source of energy.

Hydrogen is a readily available gaseous source provided it can be stored and handled safely. I have worked with scientists at Oak Ridge National Laboratory where I have learned that nanocrystalline metallic alloys can be processed by low temperature deposition for highly concentrated hydrogen solid-state sources. These metal hydrides are a safe alternative to the safety problems imposed by hydrogen storage in liquid and gaseous forms. Also, I have found through scientific literature that the kinetics of hydrogen desorption are very fast in nanocrystalline materials, in which these materials could be fittingly used for hydrogen storage for fuel cell applications.

## **1.8. Thesis Overview**

I provide in the next few paragraphs a brief description of the organization of the thesis. The thesis consists of two main thrusts. The first part is to show the feasibility of achieving nanocrystalline grain size in the films by performing low temperature deposition, while the second part is to show the effect of nanocrystalline grain size on the capacity to store hydrogen.

We have chosen zirconium and titanium as the two compositions of the films to deposit as these are known to be hydride forming. Deposition of these films by magnetron

sputtering follows a simple procedure with the readily available targets in our laboratory. Although other elements such as magnesium would have been advantageous from consideration of higher weight percent hydrogen that can be stored, the strong tendency to oxidation deterred us from making this choice. In fact, our results showed that low temperature deposition of titanium in the simple experimental set up was also responsible for oxidation of the films. Desorption of gaseous species such as oxygen is favorable only at higher temperatures. In addition, continuous deposition of the films allows oxygen to be depleted from the plasma initially so that the total oxygen content is less. The temperature of the substrate that was taken to  $-50^{\circ}\text{C}$  rose quickly in the plasma so that deposition has to be interrupted for cooling. This interruption by as much as 15 minutes between depositions of 1 minute allowed oxygen to be absorbed again in the films. Deposition of the films could have been carried out at much lower temperatures with a smaller substrate holder that could be cooled quickly by circulating cooled nitrogen.

Incorporation of hydrogen into the films was carried at  $300^{\circ}\text{C}$  and low pressure of 50 - 60 Torr. Molecular hydrogen charging was not very effective in terms of the quantity incorporated in the lattice, so I then used plasma charging of hydrogen. Microwave power was used to generate the plasma of hydrogen and this also increased the substrate temperature to  $300^{\circ}\text{C}$ .

I have used polished silicon and porous aluminum oxide filters as the substrates for deposition of the films. Deposition on silicon enabled X-ray analysis to be quantitative in

terms of grain size determination and peak shift analysis. Results of deposition on porous alumina were helpful in identifying the morphology of the films on high surface area porous substrates. Quantitative analysis of hydrogen by any other techniques other than secondary ion mass spectrometry was not very conclusive as the thickness of the films was close to 0.5  $\mu\text{m}$  and the mass fraction of hydrogen was low. For the same reason, investigation of desorption kinetics of hydrogen from the films also was not conclusive. Valuable information of the nanocrystalline grain size of the films was obtained from the films deposited on carbon holy grids. Deposition of the films for short periods enabled direct examination of the samples in the high resolution electron microscope whereby the lattice fringes in the favorably oriented nanocrystalline grains were imaged.

The presentation of the results followed the chronological order of the experiments. It became clear through the initial results of electron microscopy that nanocrystalline grains were obtained. It was also found that this nanocrystalline grain size microstructure is stable even after heating to 300°C. X-ray analysis on silicon substrates also showed smaller grain size at lower temperatures, however, quantitative grain size gave a higher value than was observed directly from lattice fringes. I anticipated the hydrogen charged samples to exhibit peak shifts of the X-ray reflections. However, it became clear that the absence of peak shifts in the peak positions is an indication that little hydrogen is present in the lattice and much remained along the grain boundaries. This result is consistent with many observations wherein the changes in the lattice parameter in the presence of hydrogen in the solid were insignificant.

Secondary ion mass spectrometry showed clearly that the hydrogen concentration in the smaller grain size nanocrystalline films was an order of magnitude higher compared to that in the films with larger grain size. The resolution of the instrument was not large enough to show the higher concentration at the grain boundaries as the nanocrystalline grain size was much smaller than the beam size.

Electrical resistivity measurements were also performed to show the changes arising from the difference in the hydrogen concentration. As resistivity change could arise from decrease in grain size, increase in incorporation of oxygen and hydrogen, the results were viewed cautiously. I have assumed oxygen concentration to remain constant among each sample.

The kinetics of desorption was very difficult to observe as I now believe the quantity of desorbed hydrogen is very small and did not give rise to enough pressure changes in the system employed. Lack of an automatic Sievert's apparatus in the laboratory as well as the high temperature of desorption of hydrogen in zirconium contributed to the difficulty. Finally, other than the high resolution microscopy of nanocrystalline grain size of titanium, a major part of the thesis is based on the results obtained from zirconium films. Oxidation of titanium films did not allow many of the experiments to be conclusive.

## 2. EXPERIMENTAL

### 2.1. Materials and Sample Preparation

Zirconium and titanium nanocrystalline films in this work were deposited on three types of substrates: porous alumina filters, carbon-lacy grids, and silicon wafers. The porous alumina filters, *Anodisc filters*, were purchased from Whatman International Ltd, Maidstone, England, while the carbon-lacy grids were purchased from TED PELLA INC.

All silicon wafers used as substrates were first cut to the desired size using a diamond scribe, and then cleaned with acetone and etched with hydrofluoric acid to remove any surface native oxide and impurities on the surface. Post coating deposition handling required that the porous alumina substrates, each 2 cm diameter alumina filter be taped to a cleaned silicon wafer with scotch tape, due to sample brittleness. The tape was applied in four places to the polymer ring that encircled the filter, as seen below in figure 2.1.

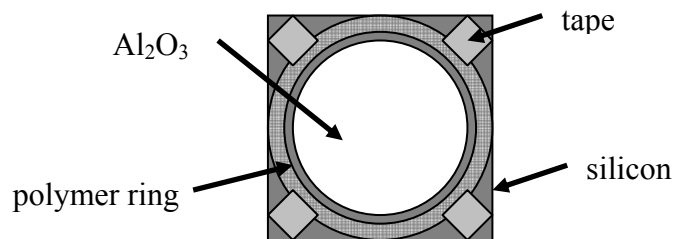


FIGURE 2.1. Porous alumina substrate taped to silicon.

Similar to the filters, the 2 mm diameter carbon-lacy grids were also taped to silicon before deposition to prevent the grids from falling off the substrate holder.

## 2.2. Physical Vapor Deposition

A magnetron sputtering unit, schematically illustrated in figure 2.2, was used for the physical vapor deposition of the films. The system operates with reactive pulsed DC and AC magnetron sources and a unique substrate holder that enables cooling of the substrate during deposition.

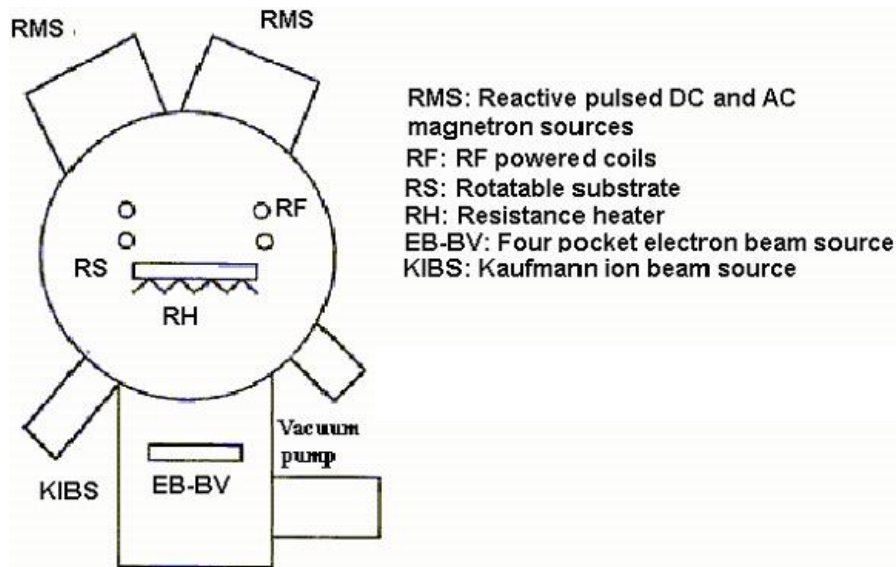


FIGURE 2.2. Magnetron sputtering unit.

The unique substrate holder was made for the purpose of performing low temperature depositions, where two bellows create a path for cooled nitrogen gas to circulate below the substrate stage. Also included on the substrate holder is a thermocouple connection, enabling accurate temperature measurements of the substrate surfaces during deposition.

Targets of titanium and zirconium are used separately for the deposition of the respective nanocrystalline films.

During both room temperature and low temperature depositions, the argon pressure in the system remained between 2 and 3 mTorr, with an average current of about 1.10 A. Also, the effective sputtering power remained at approximately 0.52 kW, while the circulating power was approximately 0.38 kW. At the beginning and end of every deposition, the chamber was flushed with nitrogen gas to prevent any moisture from collecting on the chamber walls while the chamber was open. After placing the samples on the sample stage and loading them into the chamber, the vacuum pump was opened to begin the process of creating a good vacuum in the system, and the chamber was baked at about 100°C to remove any moisture in the chamber. Upon reaching a vacuum of  $5 \times 10^{-6}$  Torr, the DORA power system was used to generate the plasma via pulsed DC current. When the argon pressure was around 2-3 mTorr, the pulsed DC power was started to generate the plasma with the current at zero amps. Then, the current was slowly increased to about 110 A, which automatically attuned the effective and circulating power to 0.52 kW and 0.38 kW respectively. During deposition, the multi-meter connected to the thermocouple was monitored to measure voltage and temperature of the substrate. Due to the high temperature of the plasma, the films were deposited in increments of time periods determined by the temperature increase of the substrate. Because the zirconium plasma generated a higher temperature than that of titanium, further and shorter increments of time were required during zirconium deposition to keep the substrate at the

lower temperature. The temperature control strategy for titanium deposition consisted of deposition for 2-3 minute increments, followed by cooling, and deposition for 11 minutes total. For zirconium, 1 minute of deposition, followed by cooling, and total deposition of 11 minutes. Eleven minutes of total deposition time was preferred to achieve the desired film thickness of 0.65-0.80  $\mu\text{m}$ .

### ***2.2.1. Room Temperature Deposition***

When depositing both the titanium and zirconium films at room temperature, no cooling source was used. When the multi-meter read 0 mV, which corresponds to 300 K, the deposition was started by generating the plasma, as described previously. To avoid deposition at high temperatures, and to keep the temperature as close as possible to room temperature, the plasma was turned off when the temperature reached 310 K for Titanium and 320 K for Zirconium, corresponding to multi-meter readings of 0.5 and 1.0 mV respectively. Once the chamber was cooled back to room temperature, after about 5 minutes, the deposition process was repeated until 11 total minutes of deposition was reached.

### ***2.2.2. Low Temperature Deposition***

Unlike room temperature deposition, low temperature deposition of titanium and zirconium required a cooling system to keep the average substrate temperature around 228 K. The cooling system consisted of circulating cold nitrogen gas through the

substrate holder. Nitrogen was cooled by passing the gas through a coil that is submerged in liquid nitrogen in a dewar, as seen in figure 2.4.

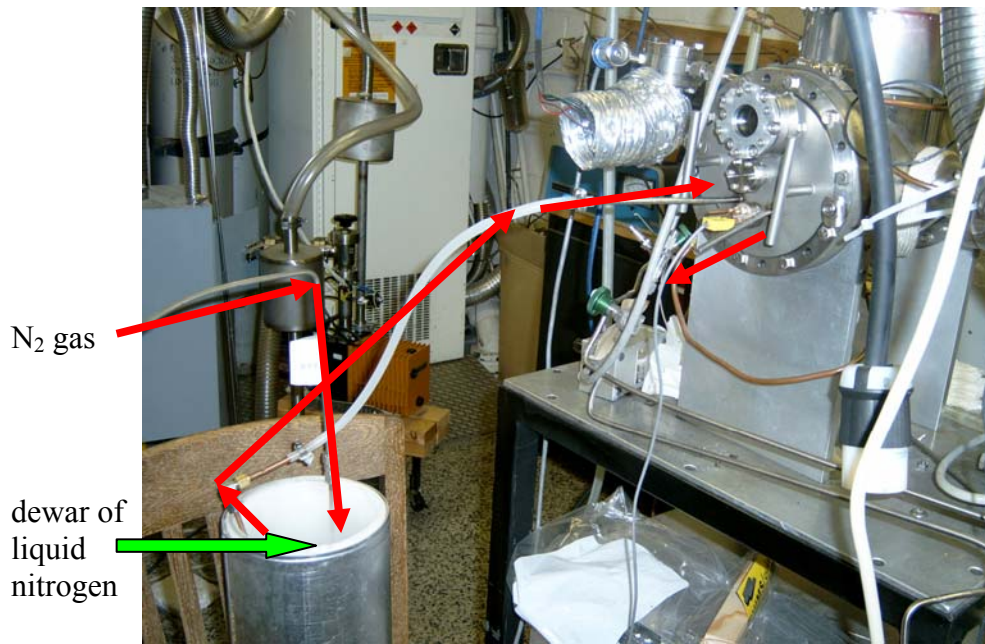


FIGURE 2.3. Cooling apparatus for low temperature deposition.

When the multi-meter read between  $-2.5$  mV and  $-2.0$  mV, which corresponds to 236 K and 248 K, the deposition was started, and it was stopped when the temperature reached about 268 K, which is  $-1.2$  mV on the multi-meter. Then, just as with the room temperature depositions, once the chamber was cooled back to room temperature, after about 5 minutes, the deposition process was repeated until a total of 11 minutes of deposition was completed. The total deposition time for the films could not be increased further as it was taking a very long time to maintain the substrate at low temperature. Certain depositions at low temperature took as much as five hours for completion.

In addition to room and low temperature depositions, some films were deposited at an intermediate or “medium-low” temperature to better track the changes in grain size associated with different deposition temperatures. These films were also deposited in increments for a total of 11 minutes.

### **2.3. Hydrogen Charging**

Two methods of hydrogen charging were employed to various titanium and zirconium films deposited at room temperature and low temperature. The first method was molecular charging, which is gaseous charging of hydrogen at 60 Torr pressure and room temperature for 3 hours. This method of hydrogen charging was carried out for some samples in the same chamber, the magnetron sputtering unit, in which the samples were deposited. The other samples were treated in the ASTEX (Applied Science and Technology, Inc.) microwave plasma chamber. The samples were simply placed on a substrate holder, loaded into the chamber where the chamber was evacuated and hydrogen gas was introduced to a pressure of around 60 Torr. The samples remained in the hydrogen atmosphere for 3 hours before the gas was turned off, at which point the samples were removed without reduced chamber pressure.

In addition to molecular charging at room temperature, some samples were also hydrogen charged via molecular charging at a higher temperature of around 573 K (300°C), with a pressure of 50 Torr and hydrogen flow rate of 7 sccm for 3 hours. The purpose for charging at a higher temperature was to increase the diffusion of hydrogen into the films.

This was done in the ASTEX microwave plasma chamber, and the substrate temperature was controlled by resistance heating using the Sorensen DCR 20-115B Power Supply. After charging for 3 hours at 573 K, the temperature was slowly decreased back to room temperature, and then the hydrogen flow was stopped.

The second method of hydrogen charging was ionic charging, which consists of microwave-generated hydrogen plasma charging at 10 Torr pressure for 2 hours with about 300 watts of energy. The plasma charging began at room temperature, and then increased to 573 K by the end of the 2 hours due to the high temperature of the plasma. This method of charging was executed in the ASTEX microwave plasma chamber, and the plasma was controlled by the ASTEX S-1500i Microwave Plasma Generator.

It is important to note that ionic charging of hydrogen was only performed on the films that were deposited on silicon substrates because the high temperature plasma could “calcify” the alumina filters.

## **2.4. X-ray Diffraction**

X-ray diffraction was performed on several samples deposited on silicon and porous alumina substrates. Initial diffraction measurements were taken on silicon supported substrates with the RIGAKU instrument at NCSU to verify elemental information, while further measurements were taken on the PANalytical XPERT MPD X-ray Diffraction system and the SCINTAG Rotating Anode in the High Temperature Materials Laboratory

(HTML) at Oak Ridge National Laboratories (ORNL) with Thomas Watkins. Since the samples on the alumina substrates do not have a flat surface, these samples were measured with a parallel beam optics on the PANalytical system, which eliminated peak shift due to sample surface displacement. Most of the silicon supported samples were measured on the SCINTAG PIS rotating cathode diffractometer with 4-axis goniometer, which has much higher flux, resulting in enhanced diffracted intensity. Both of the diffraction systems used a Cu  $K_{\alpha}$  radiation source with  $\lambda = 1.540593 \text{ \AA}$ . The current supplied with the RIGAKU was 25 mA, while that for the PANalytical system was 40 mA, and for the SCINTAG 300 mA. Diffraction intensities were measured every  $0.02^{\circ}$  (step size =  $0.02^{\circ}$ ) from  $2\theta = 20^{\circ}$  to  $80^{\circ}$  at a rate of 10s/step, so about 8 hours per run.

The purpose for doing the diffraction experiments was for phase identification and relative crystallite size determination associated with changes in peak position and width respectively. The characteristic peaks of interest are centered at  $2\theta = 31.7^{\circ}$ ,  $34.5^{\circ}$ , and  $66.3^{\circ}$  for zirconium; at  $2\theta = 34.5^{\circ}$ ,  $56.4^{\circ}$ , and  $62.1^{\circ}$  for zirconium hydride ( $ZrH_{0.25}$ ); and at  $2\theta = 35.2^{\circ}$  and  $38.3^{\circ}$  for titanium.

In addition to diffraction experiments on the nanocrystalline films, a diffraction run on “As-received Zr powder” was conducted using the PANalytical system for the purpose of attaining a standard in which full width at half maximum (FWHM) experimental values could be properly adjusted for instrumental broadening.

## 2.5. Resistance Measurements

Resistance measurements were taken with a system comprising a Keithley 2400-LVSourceMeter, a Keithley 2182-Nanovoltmeter, a K-20 Temperature Control System and a low temperature chamber both from MMR Technologies Inc., and HTBasic software, which was programmed by Jag Kasichainula. The sourcemeter was used to apply a current of 1 mA, while the nanovoltmeter was used to monitor the voltage in the system. The given current with the measured voltage was used to generate the resistance measurements with Ohm's Law;  $V = IR$ . The K-20 Temperature Control System enabled the runs to range between room temperature at 300 K and a lower temperature at 165 K, while capturing resistance measurements every 4 degrees Kelvin. The test operated under a 6 mTorr vacuum, and the dewar was cooled by adiabatic expansion of nitrogen gas flow that remained around 3.4 sccm, under a pressure of 1800 psi. The outputs from these tests are in the form of graphs of resistance as a function of temperature.

The resistance measurements were performed on samples containing nanocrystalline zirconium films on silicon substrates with a combination of deposition temperatures and hydrogen treatments for characterization of hydrogen capacity. The presence of hydrogen reduces the mobility of electrons by means of scattering, and in effect, this scattering from hydrogen increases resistivity of the material. The resistance measurements as a function of temperature were sensitive to hydrogen because vibrations in the lattice decrease with decreasing temperature, in turn showing impurities such as hydrogen much more clearly.

The sample preparation required for performing these tests began by cutting the silicon supported sample into a 1 x 2 cm rectangle. Four small dots of colloidal silver paste were applied along the diagonal of the rectangle, and then 0.025 mm diameter gold wires, about 2 cm long were attached to the silver dots. Once the silver paste was completely dried and the gold wires were secured, zinc oxide (ZnO) paste was applied to the substrate holder immediately before the sample was placed on the holder. ZnO is electrically insulating and thermally conducting, thus preventing false readings of electrical resistivity, while allowing sufficient temperature transfer from the dewar to the sample. Next, the free ends of the gold wires were connected to the capped on leads of the low temperature dewar with indium solder, which alloys well with gold. Two of the leads operate as input, while the other two operate as output. Finally, the dewar was closed, the proper connections to the inner leads for electrical measurements and the vacuum were made, and the test was performed. See figure 2.5 for a clear visual representation of the inside of the dewar.



FIGURE 2.4. Low temperature dewar for resistivity measurements.

The type of resistance test performed on the samples was sheet resistance, in which four probes were used rather than two probes to avoid false measurements from contact resistance that occurs with two probe measurements. Rather than directly measuring resistance, as done with two probe experiments, sheet resistance involves measuring the voltage over a particular area, and then calculating resistivity from the measured parameters of resistance and film thickness. As the films deposited in the present work were almost of the same thickness, sheet resistance was taken as a measure of resistivity of either Zr or Ti containing different concentrations of hydrogen.

## **2.6. Microscopy**

### ***2.6.1. Optical Microscopy***

The room temperature and lower temperature deposited Zr films with hydrogen plasma treatment were placed in the viewing area of a CARL ZEISS optical microscope with DIC (differential interface contrast), model 60523. Optical micrographs of several places on each sample were captured using a digital camera.

### ***2.6.2. Scanning Electron Microscopy***

Al<sub>2</sub>O<sub>3</sub> and Si supported samples of Ti and Zr nanocrystalline films were mounted on double-sided, conductive carbon tape, which was then adhered to a metal stub. The metal stub was coated with a gold-palladium alloy using cold physical vapor deposition to minimize any charge on the samples. The samples were then placed in either the Hitachi S-3200N SEM chamber at North Carolina State University or the Hitachi HD-2000 STEM at Oak Ridge National Laboratories and examined in secondary electron mode, which is more sensitive to topography, as well as in backscattered mode, which is more sensitive to atomic number. In secondary electron mode, samples were imaged at different magnifications. In backscattered mode, EDS (energy dispersive spectrometry) spectrums were taken on the various samples.

The purpose for using Scanning Electron Microscopy was to identify the different elements present in the films by means of x-ray mapping, line scan, and energy dispersive spectrometry, as well as to examine the porous nature of the films. SEM was also used as

an indirect method for hydride characterization, in which proposed hydride features were scanned for signs of oxygen and carbon.

### ***2.6.3. Transmission Electron Microscopy***

C-lacy grids with nanocrystalline films of titanium and zirconium were examined in the Hitachi HF-2000 FEG-TEM in the High Temperature Materials Laboratory at Oak Ridge National Laboratories with Larry Allard. The HF-2000 operates with a cold field emission electron source and gives 0.24 nm resolution and 1 nm spatial resolution. The cold field emission gun is a coherent source which is necessary for high resolution TEM. Also, high resolution requires high spatial frequencies, which was met with the instruments ability to obtain 1 nm spatial resolution. High resolution TEM analysis in addition to TEM diffraction analysis was performed on each of the samples in order to determine the grain sizes in the nanocrystalline films deposited at different temperatures.

For HRTEM, the grids were placed in the specimen holder and then loaded into the TEM. The microscope was then aligned according to standard alignment procedures. Care was also given in correcting the objective lens astigmatism, and checking the condenser lens astigmatism and beam tilt alignment. Finally, images were captured between 30K and 300K magnification on various locations along the sample.

TEM diffraction ring patterns were obtained similarly to the HRTEM images. Once the sample was loaded into TEM, the microscope was aligned according to standard

alignment procedures. Upon locating the area of interest on the sample, the instrument was switched over to the selected area diffraction mode, where the diffraction patterns were captured.

## **2.7. Secondary Ion Mass Spectrometry**

Secondary ion mass spectrometry was used to determine the relative concentrations of hydrogen in the films, and more exactly to provide evidence that the features observed were actually hydrides. SIMS depth profiles were created in Excel using data that was obtained from the Cameca IMS 6f SIMS instrument as part of the Analytical Instrumentation Facility at North Carolina State University with Fred Stevie. The Cameca IMS 6f operated with less than 1  $\mu\text{A}$  current, a 1 to 560 amu mass to charge range, an ( $M/_M$ ) 20,000 mass resolution, an image resolution of greater than 0.5  $\mu\text{m}$  from the microscope and greater than 0.2  $\mu\text{m}$  from the microprobe, and a vacuum in the analysis chamber achieving better than  $1 \times 10^{-9}$  Torr.

The SIMS depth profile analysis was repeated on a couple of places along each sample. The sputtered region of each run was 180  $\mu\text{m}$  x 180  $\mu\text{m}$ , while a central region, 60  $\mu\text{m}$  diameter circle, of the sputtered square is where the crater was made by the cesium beam. Thus, all SIMS data collected from each run on each sample is data from a 60  $\mu\text{m}$  diameter crater.

The basis of secondary ion mass spectrometry is the bombardment from a primary ion beam on the surface of a sample, where mass spectrometry of the emitted secondary ions is the result. This process may be seen in figure 2.6, which shows the sputtering of primary ions and the secondary particles, which carry positive, negative, and neutral charges [18]. When conducting the SIMS analysis, the 60  $\mu\text{m}$  diameter circle of the sample was sputtered away, while elemental analysis as a function of depth was obtained. This information is called a depth profile.

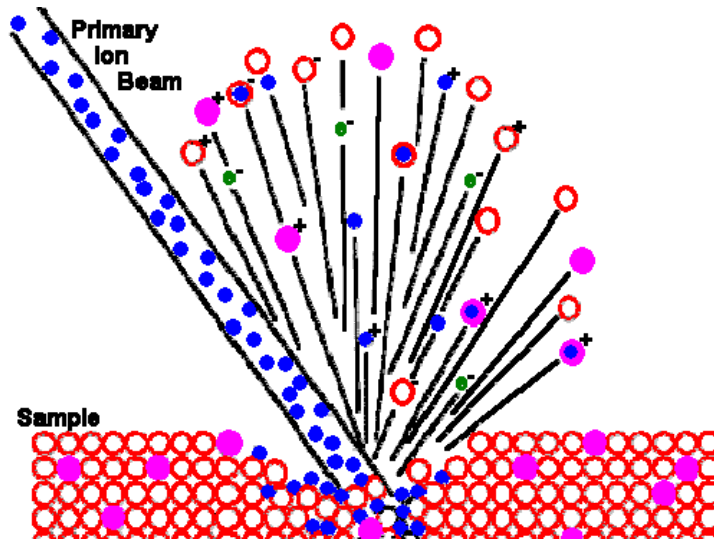


FIGURE 2.5. Diagram of SIMS operation [18].

## 2.8. Kinetics of Absorption and Desorption

The main chamber of the magnetron sputtering unit that was used for the physical vapor deposition processing was also used to test the kinetics of absorption and desorption. Samples of nanocrystalline zirconium films deposited at room temperature and lower temperature on silicon substrates with different hydrogen treatments were placed one at a time on a 4-inch diameter substrate stage. The substrate stage was equipped with a

tungsten wire heater, which allowed the samples to be heated to high temperatures, in the 500°C (773 K) range, while the Sorensen DCR 20-115B Power Supply controlled the temperature.

Once a sample was loaded, the chamber was evacuated overnight with the turbo pump and the vacuum pump running to create a vacuum of  $2 \times 10^{-5}$  Torr. Upon reaching a sufficient vacuum, the chamber was baked for one hour at about 100°C to remove any moisture in the chamber. After baking, the turbo pump was turned off and the vacuum in the system was allowed to go to  $10^{-4}$  range prior to starting the kinetics test.

Testing of kinetics began when the sample temperature was between 25°C and 100°C. Throughout the test, the temperature was slowly increased, while pressure measurements were taken at each temperature using a conductance gauge that is very sensitive to hydrogen, until temperature in the system reached about 550°C. Temperature readings were taken from a multi-meter, which directly measured voltage in mV, and the voltage was then converted to temperature, using the Chromel-Alumel Thermocouple [19]. Pressure readings were taken from a Granville-Phillips, series 275 conductance gauge, which gave pressure values in the mTorr range. The changes in pressure were then plotted as a function of temperature.

### 3. MORPHOLOGY OF NANOCRYSTALLINE FILMS

#### 3.1. Scanning Electron Microscopy

Figure 3.1 shows SEM images taken in secondary electron mode of room temperature deposited Ti film (a) and lower temperature deposited Zr film (b) on porous  $\text{Al}_2\text{O}_3$  substrates. The sample morphology images illustrate a very large surface area of the film, which is a critical factor for storing large amounts of hydrogen. The very porous nature of the substrate encourages the formation of films with rather large surface areas for the absorption of hydrogen. Since hydrogen diffusion occurs at the grain boundary region, more hydrogen can diffuse into the film through the exposed grain boundaries at the surface.

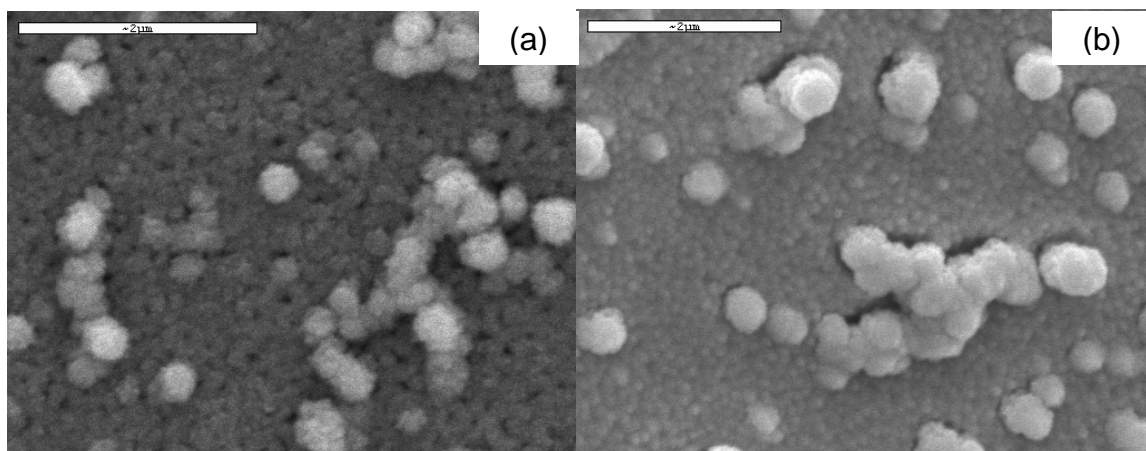


FIGURE 3.1. SEM images of room temperature deposited Ti film (a) and low temperature deposited Zr film (b) on  $\text{Al}_2\text{O}_3$  substrates, showing sample morphology.

## 4. GRAIN SIZE DETERMINATION

### 4.1. X-ray Diffraction

XRD was used to observe the changes in the phases and peak width that correspond to the changes in grain size of each sample that was deposited at different temperatures. Figure 4.1 shows broadening of a Zr peak at approximately  $2\theta = 63.5^\circ$  for the 103 reflection of Zr. The peak for the Zr low temperature line is significantly broader than those for the room temperature and medium low temperature lines, indicating smaller grain sizes for the low temperature sample.

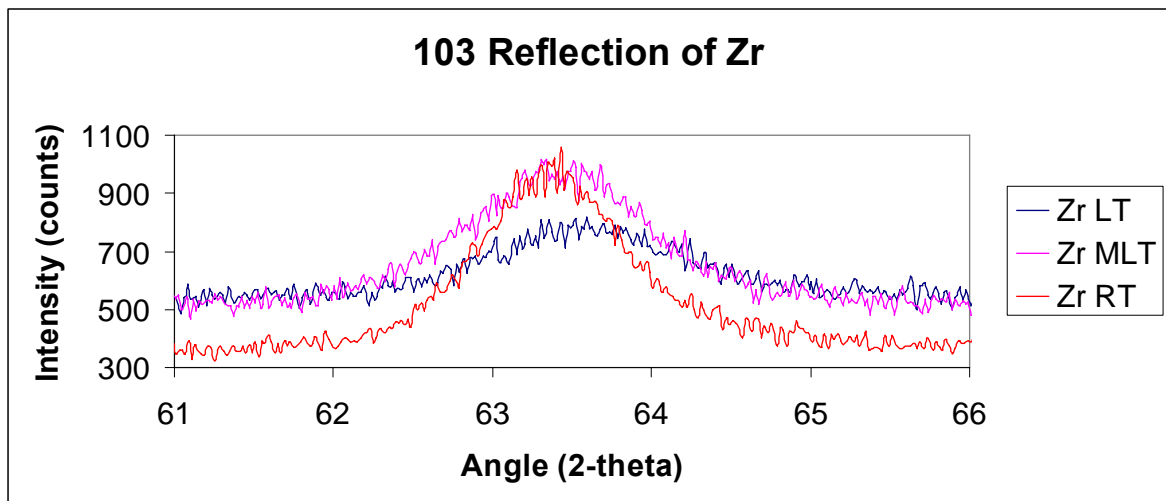


FIGURE 4.1. XRD Graph of Zr (103 reflection), showing peak broadening.

The software package “Jade” program (Materials Data, Inc, Livermore, CA) was used to calculate the full width at half maximum (FWHM) for each peak, as well as to give

information on the d-spacing corresponding to each peak. The information provided by Jade was then used in the Scherrer Formula to calculate crystallite size [20].

**Scherrer Equation:** 
$$B = \frac{0.9 \lambda}{t \cos(\theta)}$$

Where: B = FWHM (breadth)

$$\lambda = 1.5405 \text{ \AA} \text{ for CuK}\alpha \text{ radiation}$$

$$t = \text{crystallite diameter (\AA)}$$

Tables 4.1 through 4.4 contain FWHM and crystal size (XS) comparisons for the primary 2-Theta angles of each of the samples.

TABLE 4.1. Table of FWHM and XS Comparisons for Samples of Nanocrystalline Zr Films on Si Substrates, where the “Corrected FWHM” (correction due to instrumental broadening) was Employed into the Scherrer Equation to Attain Crystallite Size.

<b>Si-Zr FWHM Comparisons</b>							
Sample	2 Theta	d(A)	FWHM	Instrument FWHM	Corrected FWHM	XS (Å)	Peak Type
RT	31.760	2.8151	0.388	0.137	0.251	329.055	Zr
LT	31.752	2.8154	0.541	0.137	0.404	204.434	
RT	34.428	2.6028	0.522	0.110	0.412	201.860	Zr
LT	34.450	2.6012	0.540	0.110	0.430	193.421	
RT	66.306	1.4085	0.719	0.189	0.530	179.032	Zr
LT	66.240	1.4098	1.492	0.189	1.303	72.795	
RT MH	31.776	2.8138	0.503	0.137	0.366	225.672	Zr
LT MH	31.758	2.8152	0.522	0.137	0.385	214.526	
RT MH	34.455	2.6008	0.501	0.110	0.391	212.717	Zr + H
LT MH	34.457	2.6007	0.542	0.110	0.432	192.529	
RT MH	66.397	1.4068	0.274	0.189	0.085	1116.900	Zr
LT MH	66.234	1.3561	1.352	0.189	1.163	81.555	
RT PH	31.773	2.8140	0.441	0.137	0.304	271.696	Zr
LT PH	31.833	2.8088	0.430	0.137	0.293	281.938	
RT PH	34.583	2.5995	0.517	0.110	0.407	204.425	Zr + H
LT PH	34.617	2.5890	0.459	0.110	0.349	238.421	
RT PH	66.327	1.4081	0.792	0.189	0.603	157.377	Zr
LT PH	66.284	1.4089	1.261	0.189	1.072	88.503	

Table 4.1 shows that the FWHM slightly increased while XS decreased from the room temperature deposited films to the lower temperature deposited films. This is true for all Si-Zr samples that were treated with molecular hydrogen and for those that received no hydrogen treatments. However, two of the reflections ( $\sim 31.7^\circ$  and  $34.6^\circ$ ) for samples that were hydrogen plasma treated, indicated with blue cells, showed the opposite effect

in terms of FWHM and XS. It is very possible that this inconsistency is due to anisotropic expansion that occurs as the hydride forms. The presence of hydrogen in the lattice could be responsible for tetragonal distortion, giving rise to lattice expansion in one direction and lattice contraction in the other. It is well known that interstitial impurities are responsible for such tetragonal distortions [21]. Also, changes in FWHM of certain reflections that resulted from lowering the temperature are much less than that for other reflections taken at higher  $2\theta$  values ( $\sim 66.3^\circ$ ).

TABLE 4.2. Table of FWHM and XS Comparisons for Samples of Nanocrystalline Zr Films on Al<sub>2</sub>O<sub>3</sub> Substrates, where the “Corrected FWHM” (correction due to instrumental broadening) was Employed into the Scherrer Equation to Attain Crystallite Size.

<b>Al<sub>2</sub>O<sub>3</sub>-Zr FWHM Comparisons</b>							
Sample	2 Theta	d(A)	FWHM	Instrument FWHM	Corrected FWHM	XS (Å)	Peak Type
RT	31.990	2.7954	0.404	0.137	0.267	309.514	Zr
LT	32.121	2.7843	0.733	0.137	0.596	138.704	
RT	34.770	2.5780	0.484	0.110	0.374	222.576	Zr
LT	34.873	2.5706	0.598	0.110	0.488	170.629	
RT	36.370	2.4682	0.454	0.191	0.263	317.936	Zr
LT	36.466	2.4619	0.827	0.191	0.636	131.510	
RT	63.688	1.4599	0.128	0.184	-0.056	-1669.931	Zr
LT	63.716	1.4594	1.445	0.184	1.261	74.172	
RT MH	31.932	2.8003	0.763	0.137	0.626	131.994	Zr
LT MH	32.434	2.7581	1.026	0.137	0.889	93.063	
RT MH	34.810	2.5752	0.459	0.110	0.349	238.546	Zr
LT MH	34.925	2.5669	0.952	0.110	0.842	98.906	
RT MH	36.528	2.4578	0.432	0.191	0.241	347.117	Zr
LT MH	36.297	2.4730	1.026	0.191	0.835	100.119	
RT MH	63.568	1.4624	0.733	0.184	0.549	170.228	Zr
LT MH	63.725	1.4592	0.270	0.184	0.086	1087.615	

Similar to table 4.1, table 4.2 also shows that the FWHM increased and XS decreased slightly when the deposition temperature is reduced from 300 K to the lower temperatures. This is true for all Si-Zr samples that received no hydrogen treatment, and true for most samples that were treated with molecular hydrogen. However, the zirconium peak around 63.6 degrees for the molecular hydrogen treated sample revealed

the opposite effect in terms of FWHM and XS, indicated with blue cells. This table, table 4.2, contains no data on hydrogen plasma treated samples because this treatment could not be performed on porous alumina, as it would calcify the substrate.

TABLE 4.3. Table of FWHM and XS Comparisons for Samples of Nanocrystalline Ti Films on Si Substrates.

<b>Si-Ti FWHM Comparisons</b>					
Sample	2 Theta	d(A)	FWHM	XS	Peak Type
RT	35.23	2.54	0.46	181.2	Ti
LT	35.20	2.55	0.75	111.9	
RT	38.40	2.34	0.43	195.6	Ti
LT	38.28	2.35	0.90	93.1	
LT MH	35.21	2.55	1.26	66.0	Ti
LT MH	38.09	2.36	1.65	51.0	Ti

Table 4.3 shows that the FWHM increased while XS decreased from the room temperature to the low temperature deposited films. This statement holds true for the samples, which received no hydrogen treatment, but a comparison cannot be made for samples charged with hydrogen as no tests were run on Si-Ti samples at room temperature with molecular hydrogen treatment, and no Si-Ti samples with hydrogen plasma treatment were made. Zirconium samples have been the major focus of this work because they were not demonstrating the same obstacles with oxygen contamination as were the titanium samples, which oxidized easily as revealed in Raman Spectroscopy work at ORNL.

TABLE 4.4. Table of FWHM and XS Comparisons for Samples of Nanocrystalline Ti Films on Al<sub>2</sub>O<sub>3</sub> Substrates.

<b>Al<sub>2</sub>O<sub>3</sub>-Ti FWHM Comparisons</b>					
Sample	2 Theta	d(A)	FWHM	XS	Peak Type
RT	35.31	2.54	0.56	147.8	Ti
LT	35.33	2.54	0.40	210.5	
RT	38.34	2.35	0.48	174.9	Ti
LT	38.61	2.33	0.33	255.1	
RT	40.68	2.22	1.28	66.4	Ti
LT	40.35	2.23	0.19	452.6	
RT MH	34.81	2.58	0.65	128.7	Ti
LT MH	35.37	2.54	0.36	233.6	
RT MH	39.04	2.31	0.23	366.5	Ti
LT MH	38.45	2.34	0.29	291.1	
RT MH	39.04	2.31	0.23	366.5	Ti
LT MH	39.72	2.27	0.27	315.2	

Rather different from tables 4.1 through 4.3, table 4.4 reveals the opposite phenomenon in which the FWHM decreases while XS increases from the room temperature to the low temperature deposited Ti films on porous alumina. It was not possible to get large angle ( $2\theta$ ) reflections for the Ti films deposited on Si and Al<sub>2</sub>O<sub>3</sub>. The oxygen contamination was responsible for the peaks at higher  $2\theta$  angles to be very weak. Larger thickness of the films could have helped the peaks to appear. However, the deposition time at low temperature to get larger thickness would be very long and could not be carried out.

## 4.2. Transmission Electron Microscopy

### 4.2.1. High Resolution TEM

High resolution TEM was used to determine the grain size in the films deposited at different temperatures.

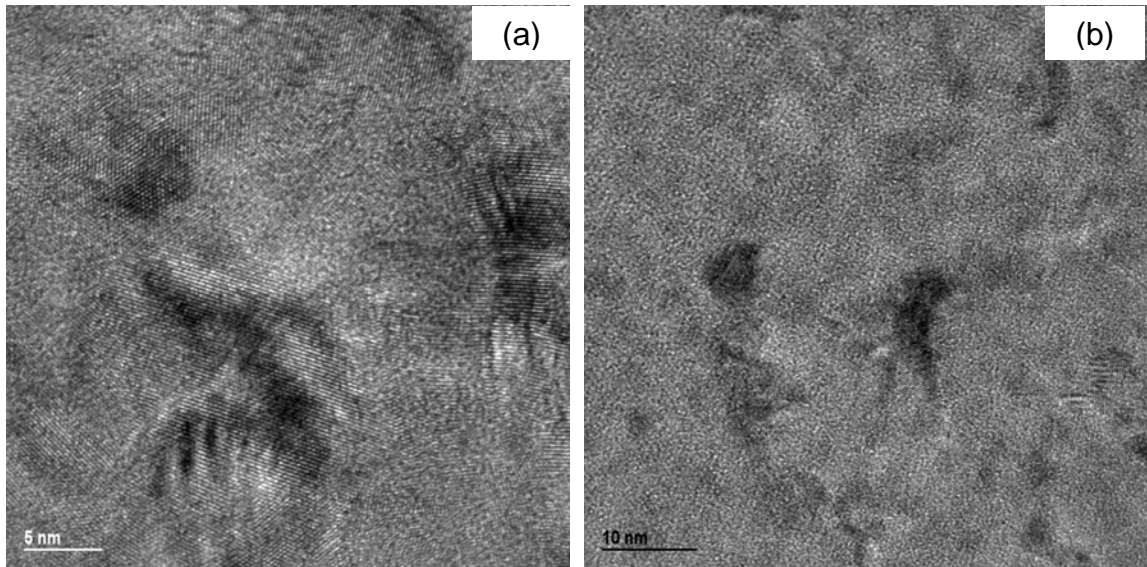


FIGURE 4.2. HRTEM image showing nanocrystalline crystallite sizes in the room temperature (a) and the low temperature (b) deposited Ti films.

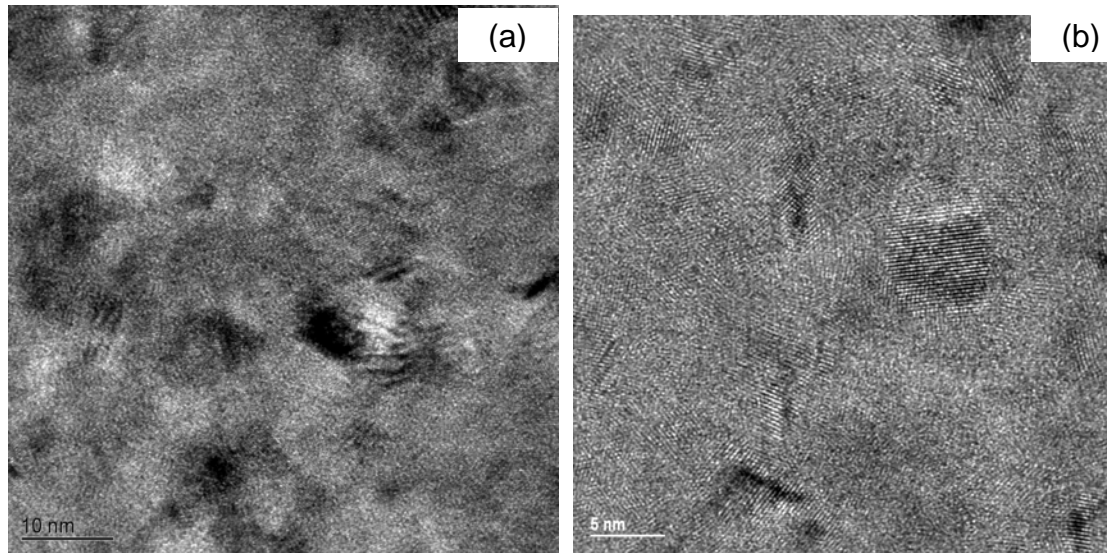


FIGURE 4.3. HRTEM image showing nanocrystalline crystallite sizes in the room temperature (a) and low temperature (b) deposited Zr films.

The average grain size determined for the room temperature deposited samples of both titanium and zirconium was between 15 and 20 nanometers, while the average grain size for the low temperature deposited films of titanium and zirconium was between 3 and 5 nanometers. These values were determined by taking an average measurement of the grain in each image.

To determine that the grain sizes were not affected by heating of the sample during hydrogen charging, additional samples of nanocrystalline zirconium films were deposited at different temperatures on carbon-lacy grids, and were then heated to 573 K for three hours, which is equivalent to the time/temperature increase observed in the samples subjected to molecular hydrogen charging. As seen in figure 4.4, the average grain size

was not affected by heating to a higher temperature. This result indicates that the microstructure is stable upon heating to 573 K.

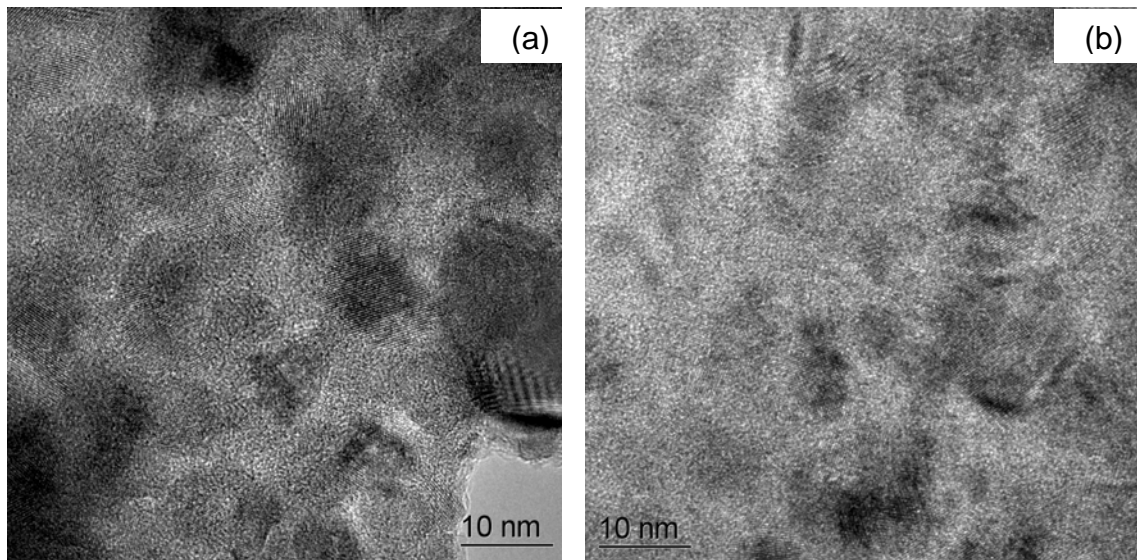


FIGURE 4.4. HRTEM image showing nanocrystalline grain sizes in the room temperature (a) and low temperature (b) deposited Zr films that were heat treated to 573 K.

The grain size data obtained from TEM was used to calculate the fraction of amorphous regions in the films, using modeling analysis of the microstructure. The average volume fraction of amorphous region in the low temperature deposited films was found to be near 23%, while that of the room temperature deposited films was found to be near 5.5%, resulting in an increase of 17% by reducing the temperature.

### 4.2.2. TEM Diffraction Patterns

In addition to using TEM for grain size determination, diffraction patterns were also taken from the TEM for each of the samples in order to make a comparison of the relative fraction of amorphous phase in the films that were made via low temperature deposition to those deposited at room temperature. The images of the TEM diffraction patterns are presented below, where broader, less defined rings are observed in the lower temperature samples, indicating smaller grain size.

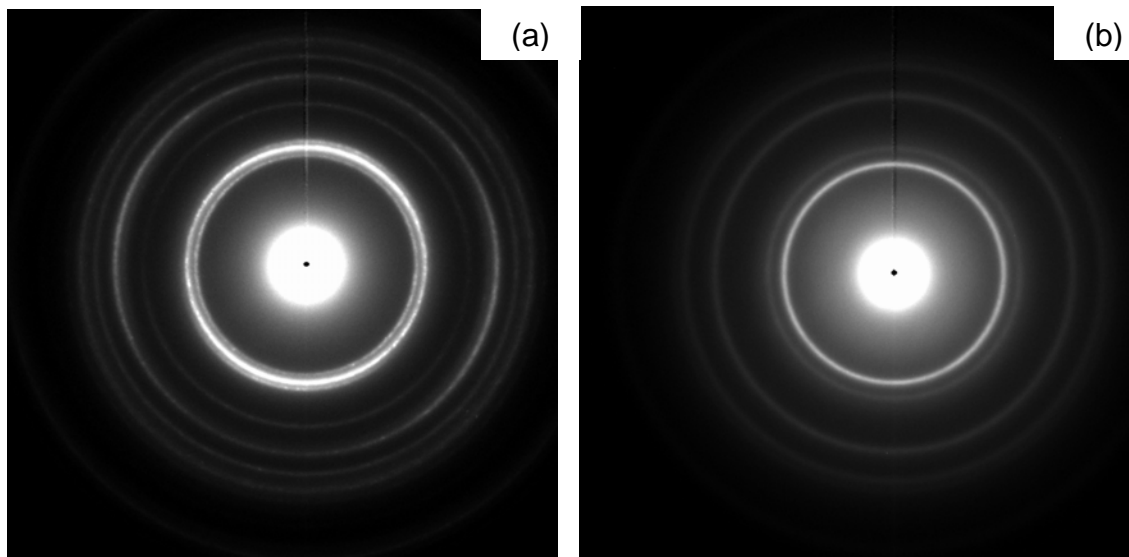


FIGURE 4.5. TEM diffraction patterns of the room temperature deposited Ti film (a) and the low temperature deposited Ti film (b).

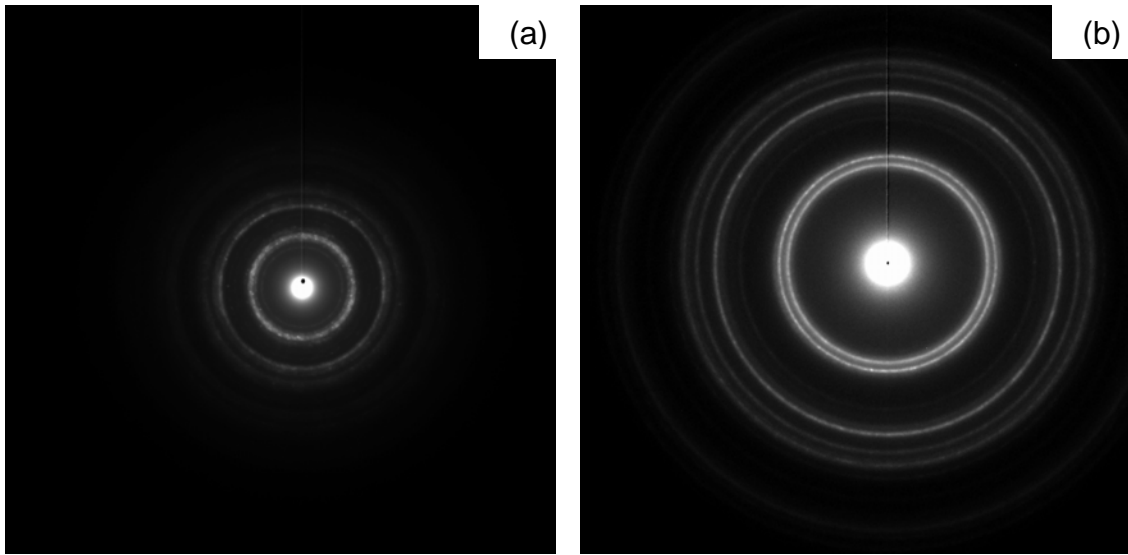


FIGURE 4.6. TEM diffraction patterns of the room temperature deposited Zr film (a) and the low temperature deposited Zr film (b).

## 5. IDENTIFICATION OF ELEMENTS AND OBSERVATION OF HYDRIDES

### 5.1. X-ray Diffraction

In addition to changes in peak breadth, XRD was also used for phase identification. Figure 5.1 provides evidence that the film is zirconium, and it also shows the presence of zirconium hydride,  $ZrH_{0.25}$ , in the low temperature, hydrogen plasma treated film.

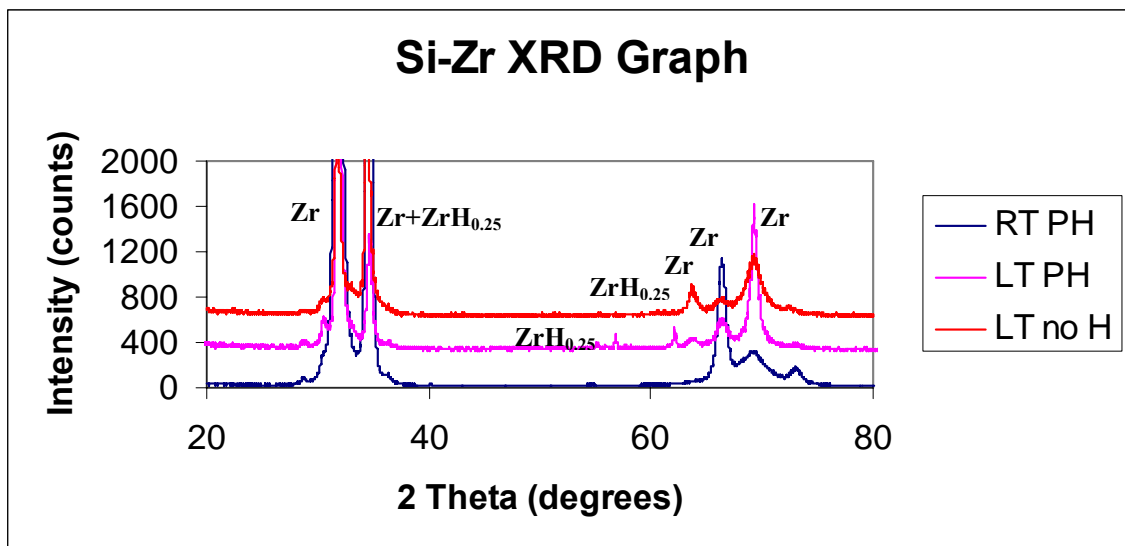


FIGURE 5.1. XRD pattern of Intensity vs. 2 Theta of Zr films on Si substrates: RT PH – room temperature deposited film with hydrogen plasma treatment; LT PH – low temperature deposited film with hydrogen plasma treatment; LT no H – low temperature deposited film with no hydrogen treatment.

Figure 5.2 also provides evidence that the film is zirconium, while illustrating the presence of zirconium hydride,  $ZrH$  and  $ZrH_2$ , around 32.2 degrees.

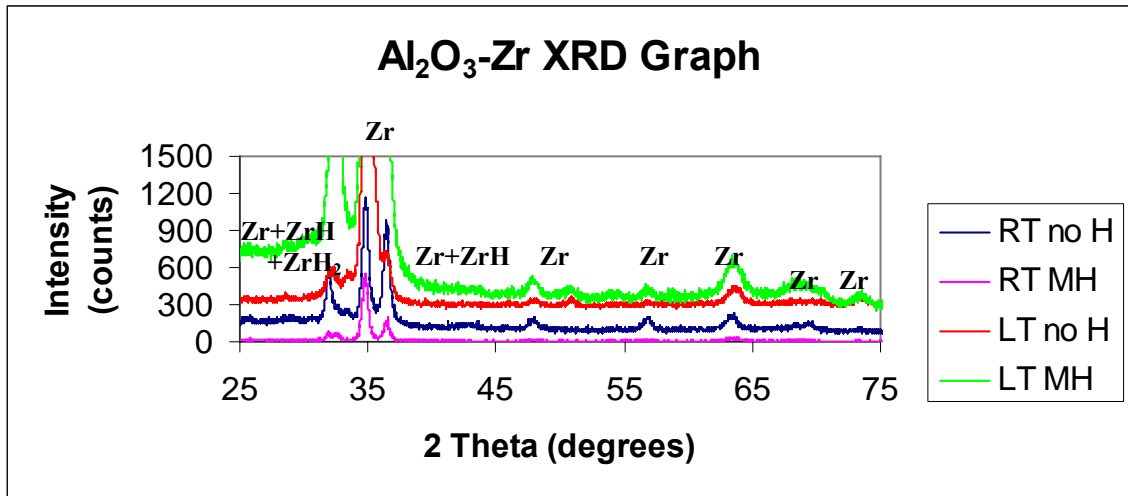


FIGURE 5.2. XRD graph of Intensity vs. 2 Theta of Zr films on Al<sub>2</sub>O<sub>3</sub> substrates: RT no H – room temperature deposited film with no hydrogen treatment; RT MH – room temperature deposited film with molecular hydrogen treatment; LT no H – low temperature deposited film with no hydrogen treatment; LT MH – low temperature deposited film with molecular hydrogen treatment.

Figure 5.3 supports that the films are titanium, but unlike the graphs for zirconium, these reveal no peaks that correspond to hydride peaks. In addition to the titanium peaks, there are several peaks between 55 degrees and 65 degrees that appear for the room temperature plasma treated films, which are representative of silicon.

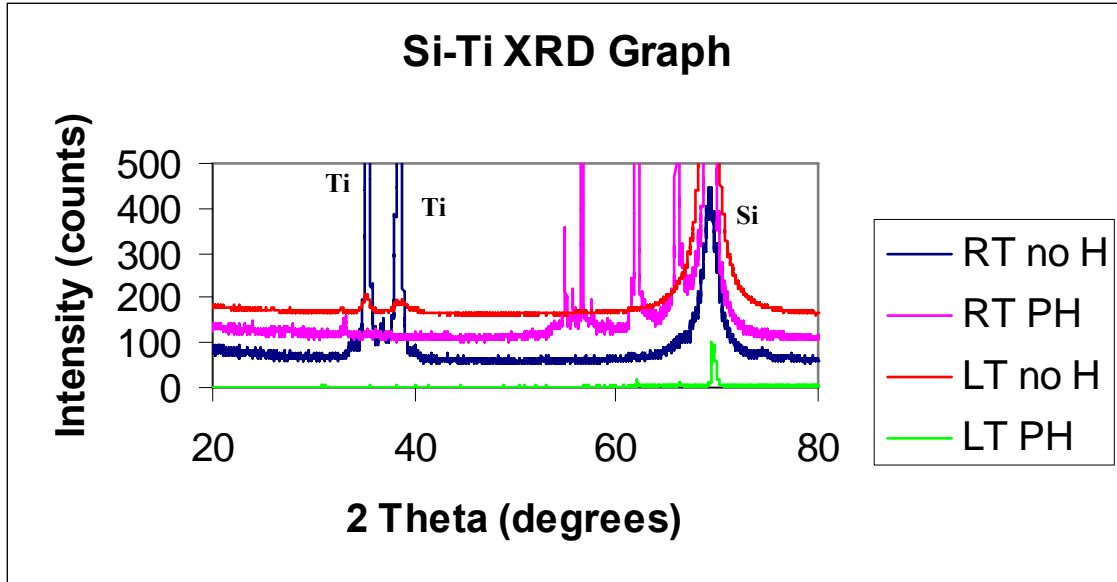


FIGURE 5.3. XRD graph of Intensity vs. 2 Theta of Ti films on Si substrates: RT no H – room temperature deposited film with no hydrogen treatment; RT PH – room temperature deposited film with hydrogen plasma treatment; LT PH – low temperature deposited film with hydrogen plasma treatment; LT no H – low temperature deposited film with no hydrogen treatment.

Just as with figure 5.3, figure 5.4 also supports that the films are titanium, but reveal no peaks that correspond to hydride peaks.

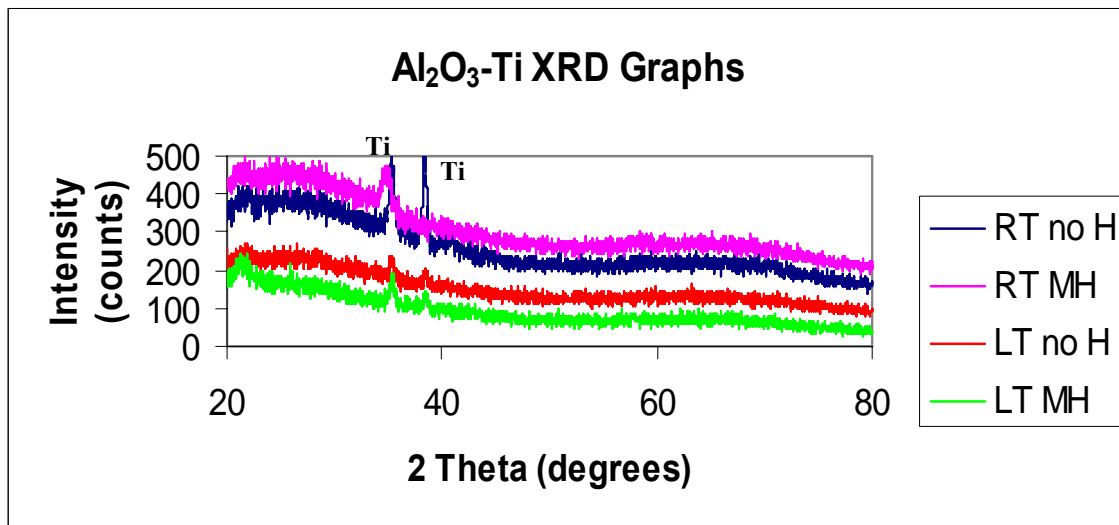


FIGURE 5.4. XRD graph of Intensity vs. 2 Theta of Ti films on Al<sub>2</sub>O<sub>3</sub> substrates: RT no H – room temperature deposited film with no hydrogen treatment; RT MH – room temperature deposited film with molecular hydrogen treatment; LT no H – low temperature deposited film with no hydrogen treatment; LT MH – low temperature deposited film with molecular hydrogen treatment.

## 5.2. Optical Microscopy

Figure 5.5 shows optical micrographs taken of plasma treated Zr films deposited at room temperature and lower temperature. As seen in these micrographs, features observed on the surface were confirmed through SEM and SIMS to be hydrides. Also depicted in the micrographs are different shapes and amounts of hydrides between the two samples. The room temperature sample (a) has fewer hydrides that are more round or “dot-like” in shape, while the lower temperature sample (b) has more hydrides that are long and “wormy” in shape. A possible reason for the difference in shape is due to the amount of

hydride formation. Since there are places on the low temperature film that have the round hydrides, it is likely that hydride formation begins as “dot-like” shapes, and then grow into the “wormy” shaped noticed in the lower temperature micrograph.

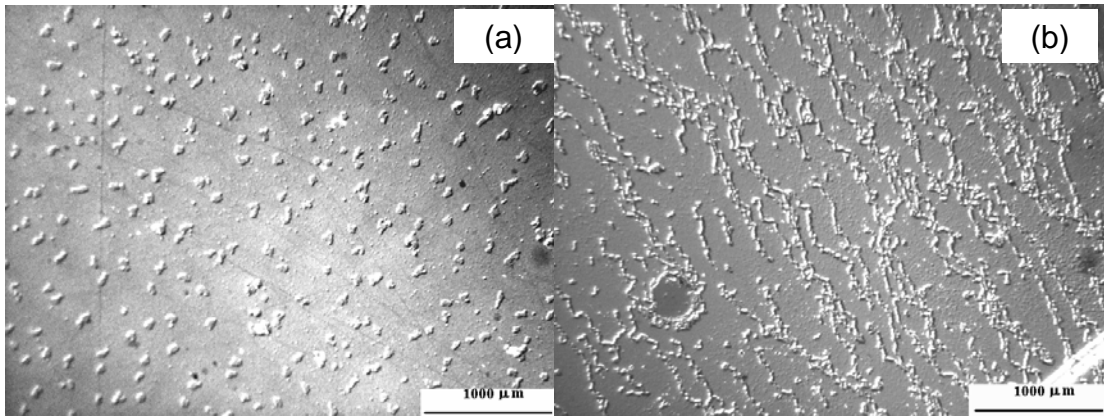


FIGURE 5.5. Optical micrographs of both the room temperature (a) and the low temperature (b) deposited Zr films on Si substrates that underwent hydrogen plasma treatment, showing presence of hydrides.

Since these shapes and quantities are not consistent throughout each sample, it is not valid to calculate area fraction of hydrides from these images.

### 5.3. Scanning Electron Microscopy

The EDS spectra in figure 5.6 validate that the films are in fact zirconium and titanium. The peak for aluminum that appears is rather insignificant to the objective of identifying elements that are present since it represents the substrate for which the films were deposited.

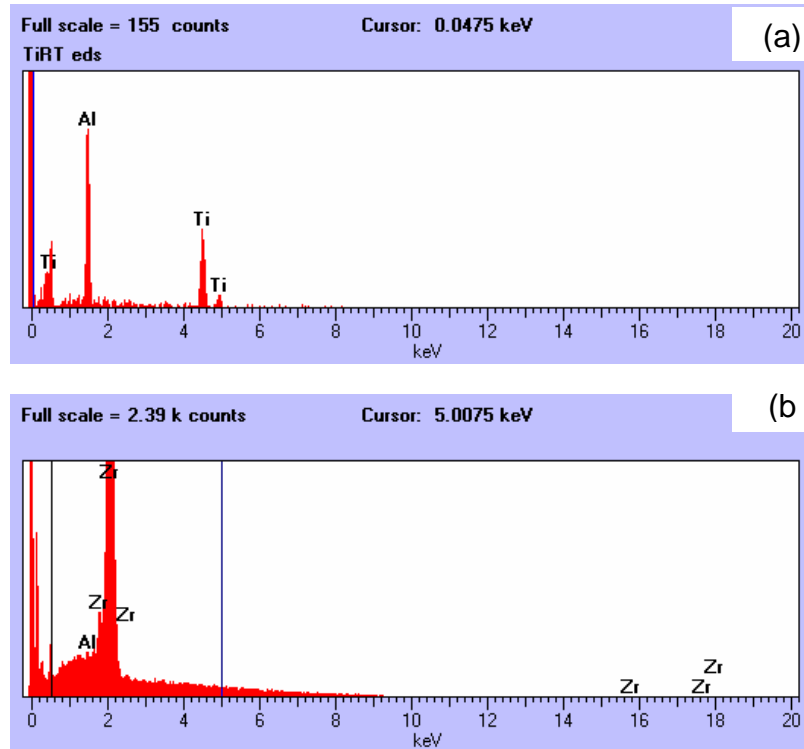


FIGURE 5.6. SEM (backscattered mode) EDS spectrums of the room temperature deposited Ti film on porous  $\text{Al}_2\text{O}_3$  substrate (a) and the low temperature deposited Zr film on porous  $\text{Al}_2\text{O}_3$  substrate(b), verifying presence of titanium and zirconium.

As seen in figures 5.7 and 5.8, SEM was also used as an indirect method of hydride characterization. SEM is considered an indirect method of hydride characterization because SEM cannot detect the presence of extremely light elements such as hydrogen. However, SEM is able to detect carbon and oxygen, which are the only other elements that could be present in the features as carbides or oxides. After conducting a line scan across the feature, the results revealed that the carbon and oxygen signals were very low, even lower than the background signal, and therefore the features are not carbides or oxides. Since the sample was plasma treated for hydrogen absorption, and SEM verified

that the defects are not oxides or carbides, the immediate assumption was that the features were hydrides. To confirm that these features were in fact hydrides, the sample was next characterized with secondary ion mass spectrometry (SIMS), which is sensitive to hydrogen.

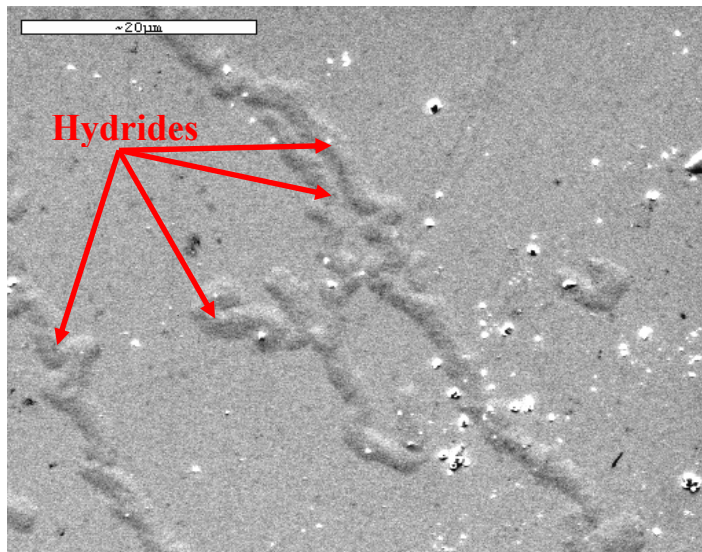


FIGURE 5.7. SEM (secondary electron mode) image of the low temperature deposited Zr film on a Si substrate that underwent hydrogen plasma treatment, showing presence of hydrides.

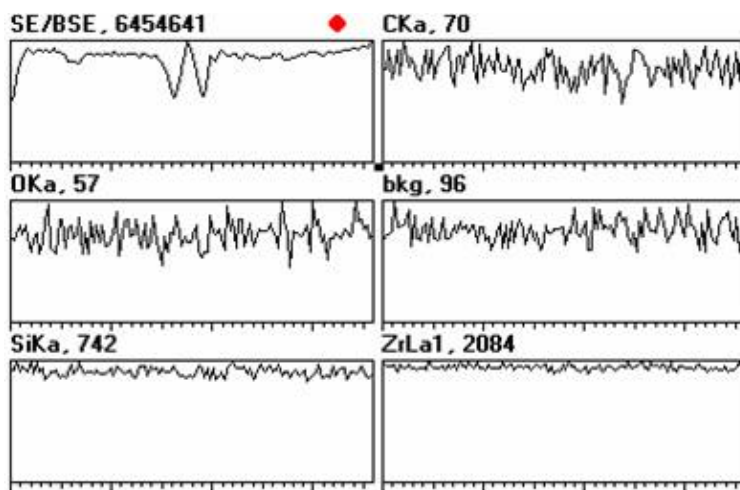
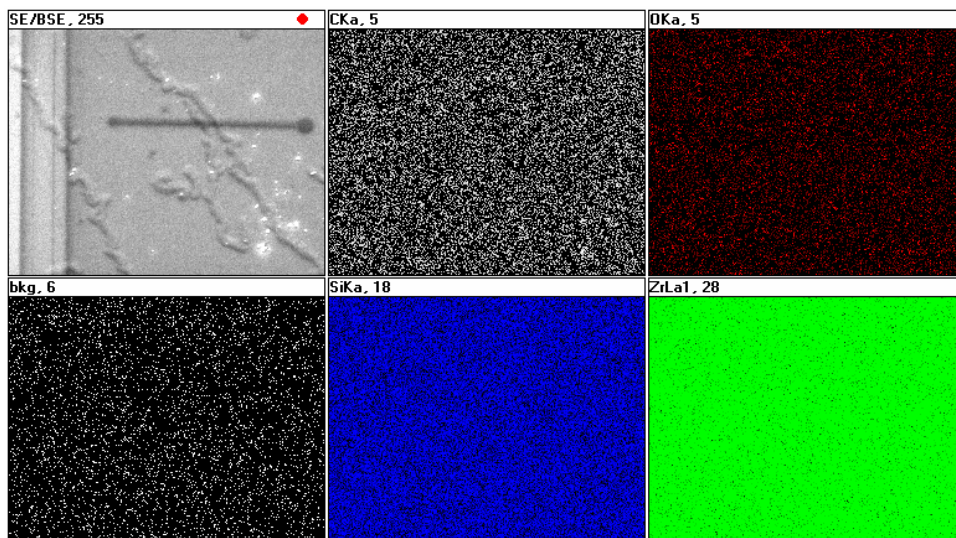


FIGURE 5.8. SEM map and line scan of the low temperature deposited Zr film on a Si substrate that underwent hydrogen plasma treatment. Starting from the top and going right to left, the k-alpha signal from carbon is 70, oxygen – 57, background – 96, silicon – 742, and zirconium – 2084.

#### **5.4. Resistance Measurements**

As seen in figure 5.9, both of the samples charged with hydrogen display a significantly higher resistance, about  $0.35 \Omega$ , than those with no hydrogen treatment, thus leading to the result that hydrogen exists in the films. Furthermore, the low temperature hydrogen treated sample exhibits a larger resistance, approximately  $0.2 \Omega$ , than the room temperature hydrogen treated sample, which supports the hypothesis that the low temperature deposited films contain a larger fraction of amorphous grain boundary region where hydrogen resides, thus increasing hydrogen concentration.

Comparing the resistance measurements of the room temperature and the low temperature deposited samples that were not treated with hydrogen, it is observed in figure 5.5 that the room temperature deposited sample has a higher resistance than the low temperature deposited sample. The logical explanation for this is that more impurities such as oxygen exist in the room temperature film due to a higher thermal energy at room temperature, thus increasing resistance.

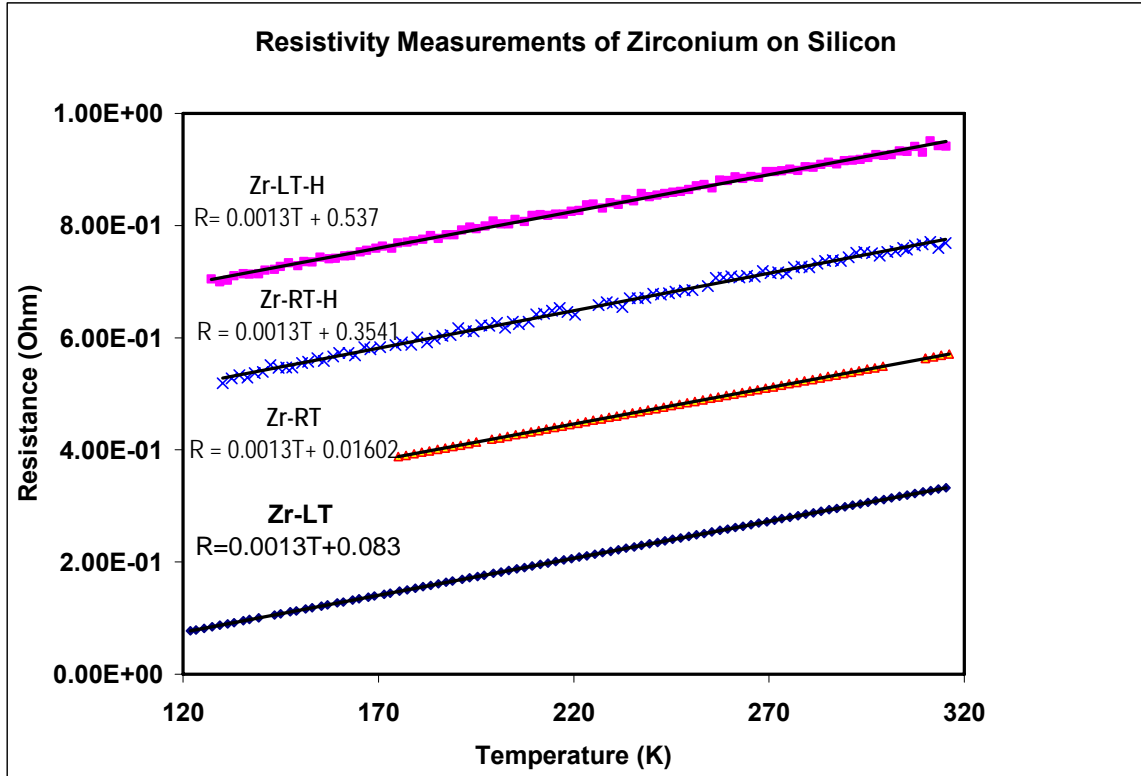


FIGURE 5.9. Graph of resistance (Ohm) vs. temperature (K) of Zr films on Si substrates: Zr-LT-H – low temperature deposited film with molecular hydrogen treatment; Zr-RT-H – room temperature deposited film with molecular hydrogen treatment; Zr-RT – room temperature deposited film with molecular hydrogen treatment; Zr-LT – low temperature deposited film with no hydrogen treatment.

Similar to figure 5.9, figure 5.10 shows that the hydrogen treated sample reveals a higher resistance, about  $0.4 \Omega$ , than the sample with no hydrogen treatment.

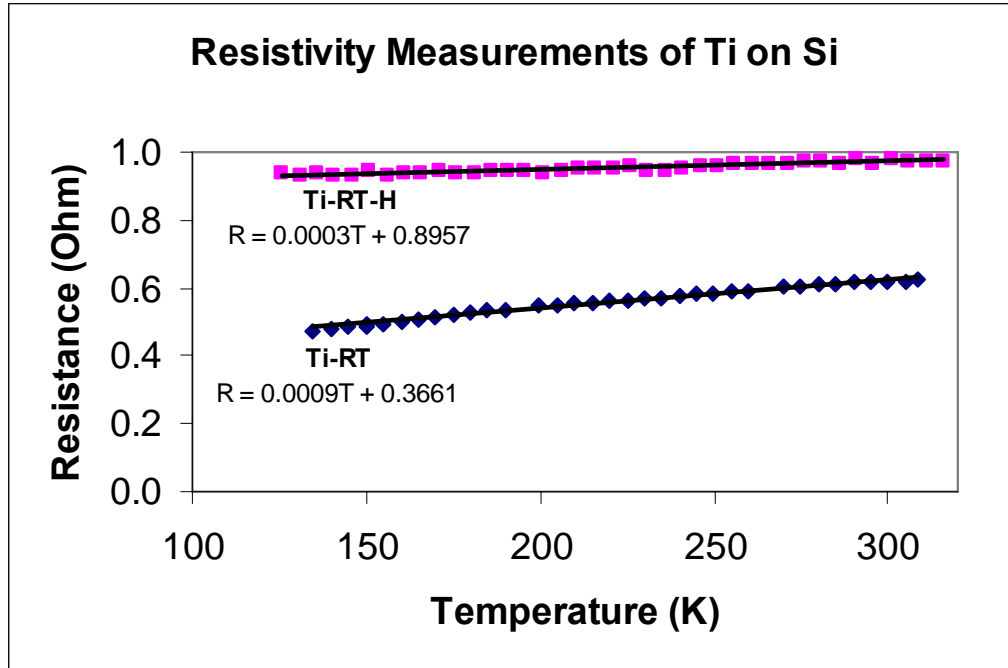


FIGURE 5.10. Graph of resistance (Ohm) vs. temperature (K) of Ti films on Si substrates: Ti-RT-H – room temperature deposited film with molecular hydrogen treatment; Ti-RT – room temperature deposited film with no hydrogen treatment.

### 5.5. Secondary Ion Mass Spectrometry

The SIMS depth profile in figure 5.11 indicates a larger concentration of hydrogen present in the samples charged with hydrogen to those that were not charged with hydrogen. The two peaks around  $1 \times 10^7$  counts/sec and  $0.05 \mu\text{m}$  depth correspond to the maximum amount of hydrogen in the samples. This maximum amount, relating to  $1 \times 10^{22}$  atoms/cm<sup>3</sup> is the saturation, which is in the form of a zirconium hydride. Beyond this maximum, the hydrogen charged samples still display higher concentrations of hydrogen than the sample that was not hydrogen charged. With the depth profile indicating the presence of hydrogen well into the film, it is evident that hydrogen

diffusion is occurring. Between 0.5  $\mu\text{m}$  and 0.65  $\mu\text{m}$  depth, another peak is observed, which corresponds to the hydrogen peak at the silicon substrate interface.

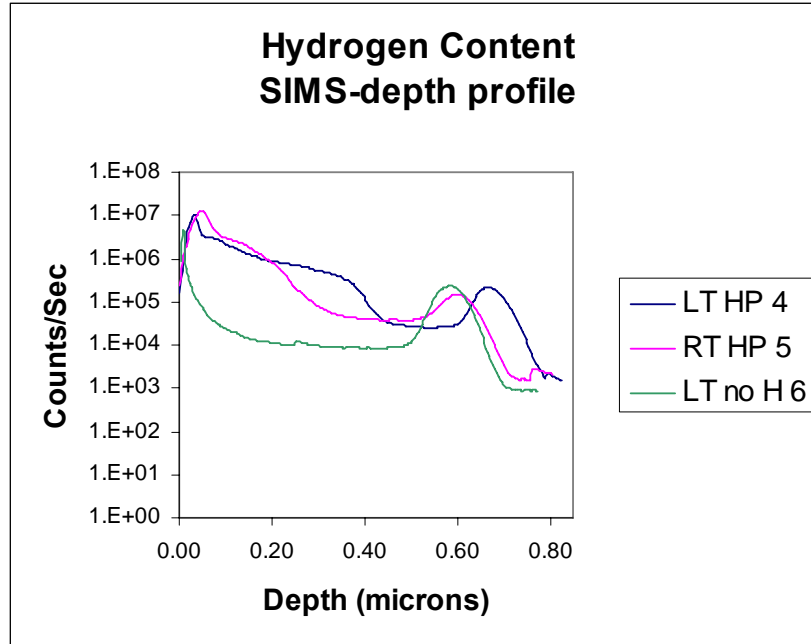


FIGURE 5.11. SIMS (secondary ion mass spectrometry) graph of counts/sec vs. depth of hydrogen content in Zr films on Si substrates: LT HP 4 – low temperature deposited film with hydrogen plasma treatment; RT HP 5 – room temperature deposited film with hydrogen plasma treatment; LT no H 6 – low temperature deposited film with no hydrogen treatment.

Figure 5.12 shows that all of the samples contain a significant amount of oxygen, which is about the same for all of the samples and to the same depths. The oscillations that occur in each curve presumably correspond to the increments of deposition time. For example, the four oscillations in the RT HP 5 sample correspond to the four increments of deposition. As deposition temperature was a large factor, the films had to be deposited

in increments to avoid a large increase in temperature due to the rapid increase in temperature of the zirconium target. So, this particular room temperature film was deposited first for three minutes, and then allowed to cool back to room temperature. Once the temperature fell back down to room temperature, the deposition continued for another three minutes, and was stopped again. This process occurred for another two increments of three and then two minutes before the deposition process was complete for that sample. During these “cooling” stages, it appears from the SIMS data that the samples are absorbing a fair amount of oxygen. This same phenomenon is observed in the other two samples, with more oscillations for more increments of deposition in the LT HP 4 sample.

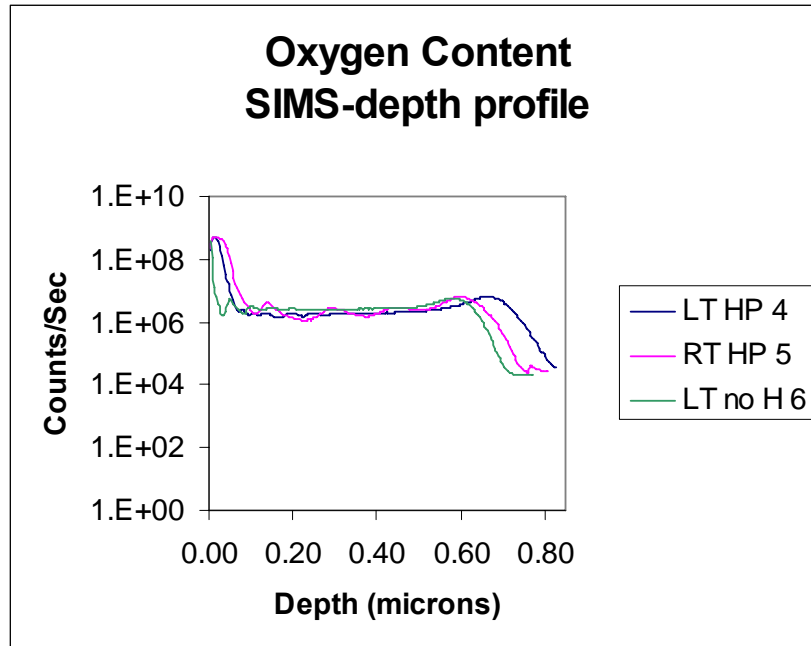


FIGURE 5.12. SIMS (secondary ion mass spectrometry) graph of counts/sec vs. depth of oxygen content in Zr films on Si substrates: LT HP 4 – low temperature deposited film with hydrogen plasma treatment; RT HP 5 – room temperature deposited film with hydrogen plasma treatment; LT no H 6 – low temperature deposited film with no hydrogen treatment.

The purpose for performing a SIMS depth profile on a hydrogen standard in figure 5.13 was to compare the known standard of hydrogen in silicon to hydrogen in the films. The hydrogen curve at  $1.5 \times 10^5$  counts/sec corresponds to  $1.5 \times 10^{20}$  atoms/cm<sup>3</sup> of hydrogen in silicon.

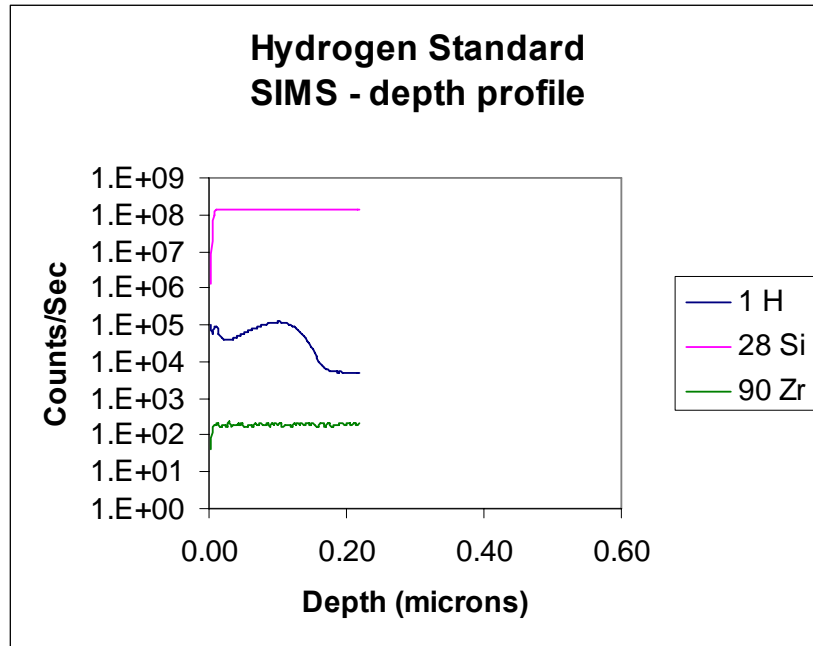


FIGURE 5.13. SIMS graph of counts/sec vs. depth of a hydrogen standard for measuring elements 1H, 28Si, and 90Zr. The standard was provided by NCSU SIMS specialist, Fred Stevie.

The hydrogen peak at  $4 \times 10^6$  counts/sec in figure 5.14 corresponds to about  $4 \times 10^{21}$  atoms/cm<sup>3</sup> of hydrogen at the surface of the film that was not charged with hydrogen.

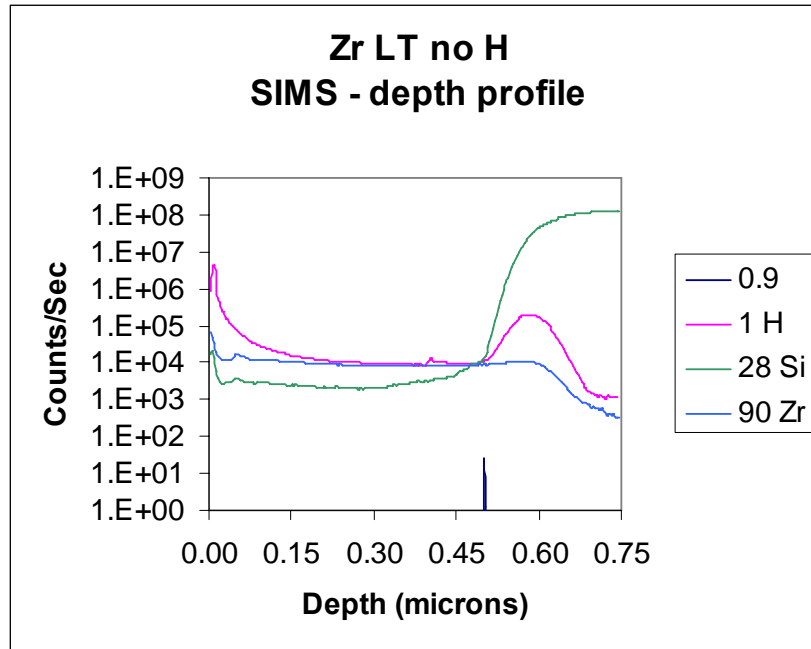


FIGURE 5.14. SIMS graph of counts/sec vs. depth of a low temperature deposited Zr film on Si substrate with no hydrogen treatment. Measurements were taken to determine presence of elements 1H, 28Si, and 90Zr.

As mentioned previously, there is a significant amount of oxygen in the films. The oxygen curve in figure 5.15 has a peak near the surface at  $4 \times 10^{23}$  atoms/cm<sup>3</sup>, but then begins to level off to  $1.7 \times 10^{21}$  atoms/cm<sup>3</sup> at 0.08  $\mu\text{m}$  depth. Also near the surface of the film, the hydrogen curve peaks at  $1 \times 10^{22}$  atoms/cm<sup>3</sup>, and lightly slopes down to  $2 \times 10^{20}$  atoms/cm<sup>3</sup> at 0.38  $\mu\text{m}$  depth. The hydrogen levels off to  $3.1 \times 10^{19}$  atoms/cm<sup>3</sup> at 0.46  $\mu\text{m}$ .

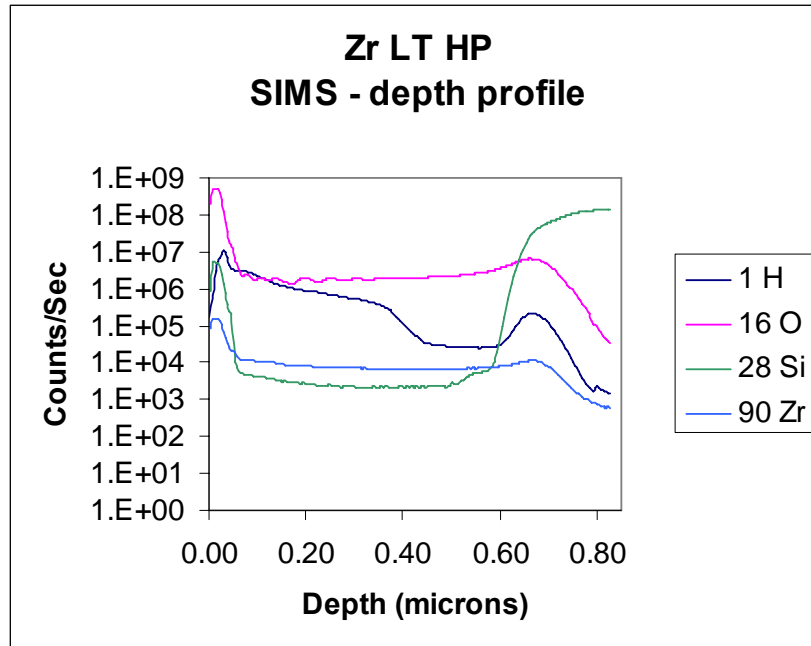


FIGURE 5.15. SIMS graph of counts/sec vs. depth of a low temperature deposited Zr film on Si substrate with hydrogen plasma treatment. Measurements were taken to determine presence of elements 1H, 16O, 28Si, and 90Zr.

In comparison to the low temperature sample in figure 5.15, the room temperature sample in figure 5.16 shows very similar profiles for oxygen, but somewhat different profiles for hydrogen, as seen in graph one. While the hydrogen curve in the low temperature film slopes down to  $2 \times 10^{20}$  atoms/cm<sup>3</sup> at 0.38  $\mu$ m depth, the curve in the room temperature film has a larger downward slope and levels off to  $4.2 \times 10^{19}$  atoms/cm<sup>3</sup> at 0.38  $\mu$ m depth. This indicates that the hydrogen content in the lower temperature film is almost one order of magnitude greater than that in the room temperature film after peaking near the surface of the film.

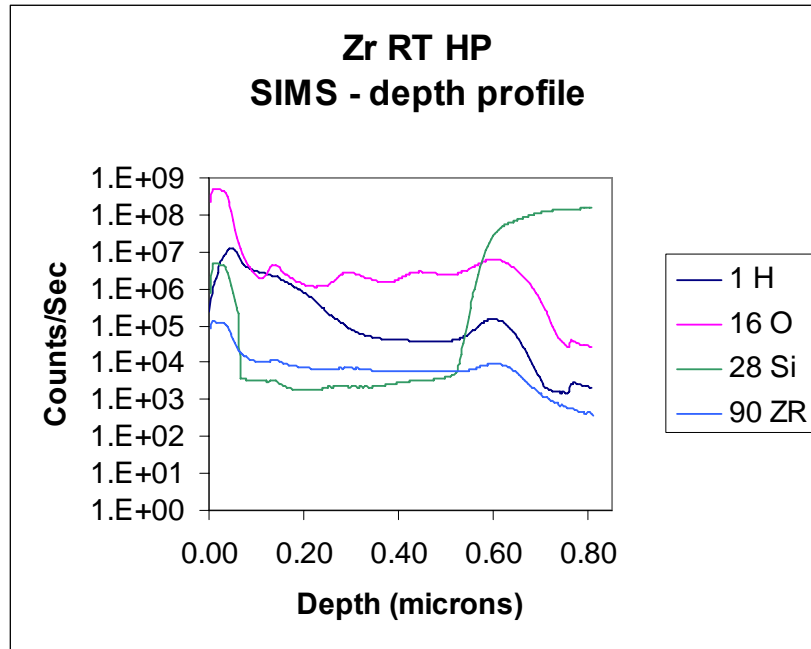


FIGURE 5.16. SIMS graph of counts/sec vs. depth of a room temperature deposited Zr film on Si substrate with hydrogen plasma treatment. Measurements were taken to determine presence of elements 1H, 16O, 28Si, and 90Zr.

It is important to note when observing these graphs that the peaks and sloping regions of the curves indicate non-uniform amounts of hydrogen, while the flat, “leveled” regions indicate uniform amounts of hydrogen. The non-uniform amounts of hydrogen are due to hydrides that are visible at high magnification in the SEM image (figure 5.7) as well as in the optical micrographs (figure 5.5). The electron multiplier image on the SIMS instrument revealed non-uniform patterns that indicated non-uniformity of hydrogen. When SIMS was performed on the regions of the films in which hydrides were visible, the electron multiplier showed non-uniformity of hydrogen, while examination of the

regions where hydrides were not visible showed uniform levels of hydrogen. This means that the features noted in SEM analysis are in fact hydrides.

## 6. KINETICS OF ABSORPTION AND DESORPTION

### 6.1. Pressure versus Temperature Measurements

In accordance with the ideal gas law,  $PV = nRT$  [22], where  $P$  = pressure,  $V$  = volume,  $n$  = number of moles of gas,  $R$  = universal gas constant =  $8.3145 \text{ J/mol K}$ , and  $T$  = temperature, a test was employed to determine increases in pressure from hydrogen desorption as a function of temperature. The volume remained constant from one test to the next for each sample so that the only variable parameters were pressure, temperature, and number of moles of gas. Pressure is proportional to temperature, and with all other values constant, an increase in temperature causes an increase in pressure and vice versa. Therefore, if gas molecules were not introduced into a system, and the temperature was increased, an increase in pressure in a linear manner would be observed as seen in figure 6.1.

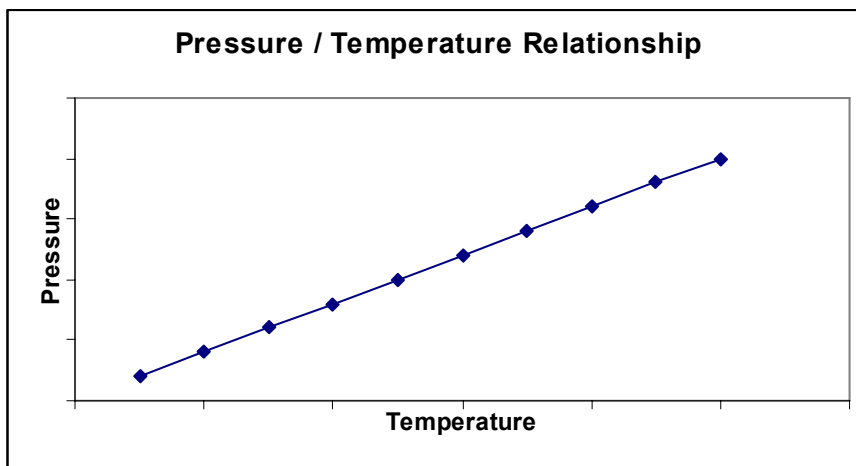


FIGURE 6.1. Generic graph of pressure versus temperature to illustrate parameter relationship.

Since pressure/temperature kinetics tests were performed on a non-hydrogenated sample and samples that were charged with hydrogen, a linear relationship, similar to that in figure 6.1 was expected for the non-hydrogenated sample, while a peak in pressure at some temperature relating to the desorption of hydrogen gas was expected for the samples which were charged with hydrogen. From the results displayed in figure 6.2, no such peak in pressure was observed in the hydrogen charged samples, with the exception of the nanocrystalline zirconium film that was deposited at room temperature and received molecular hydrogen treatment. Relative to the roughly linear relation of all other samples, response of the RT MH (room temperature with molecular hydrogen) plot reveals a peak in pressure of 465 mTorr at a temperature of 708 K (435°C). Although a peak is present, it is rather insignificant in terms of hydrogen desorption kinetics, as the rise in pressure is most likely a result of contaminants such as moisture and oxygen from the sample stage, since this RT MH run was the first run in which this sample stage was used.

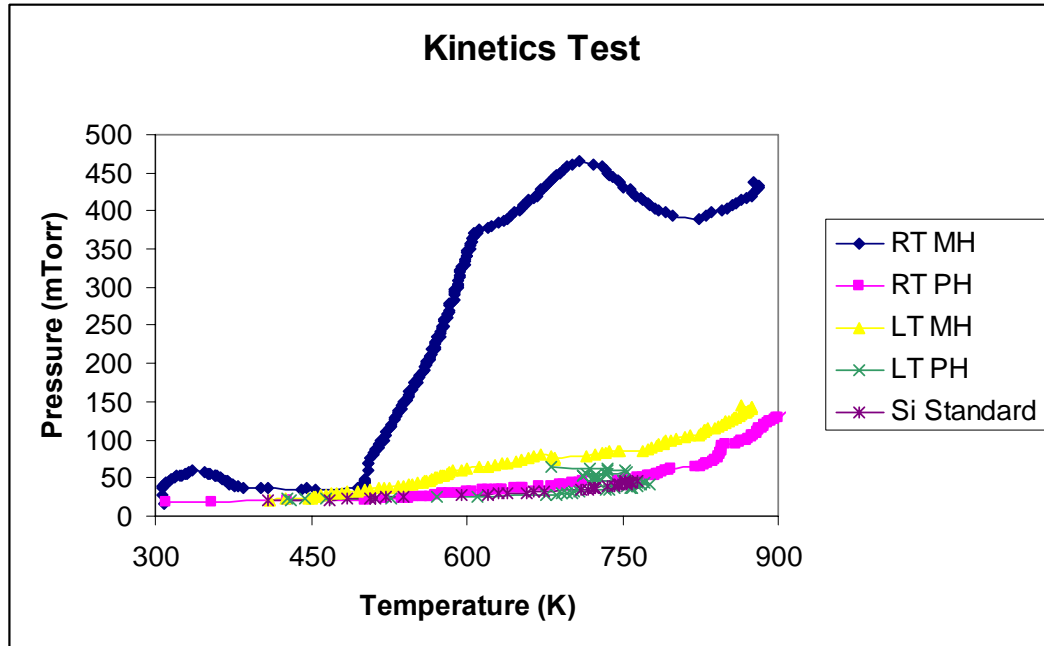


FIGURE 6.2. Pressure vs. Temperature graph of nanocrystalline zirconium samples on silicon substrates with different deposition temperatures and hydrogen treatments.

A Sievert's apparatus would have been ideal for measuring isotherms of the metal hydride samples, but no such equipment was available. For a true representation of kinetics, pressure-composition-temperature isotherms (PCT) would be essential.

Aside from testing kinetics with an available piece of equipment rather than with a Sievert's apparatus, the results are rather unrepresentative of the temperature at which desorption occurred due to the extremely low weights of the films with even less weight of hydrogen. The average weight of the films was 0.6 mg. Therefore, optimistically speaking, even if the hydrogen content in the films were 7 wt %, the weight of hydrogen

in the films would be less than 0.05 mg, which would be very difficult to detect with the method of kinetics testing that was used.

## 7. MODELING

### 7.1. Volume Fraction of Amorphous Grain Boundary Region

#### 7.1.1. Cubic System

As it is well established that a large amount of grain boundary area provides fast diffusion paths for hydrogen [23], a mathematical model for determining the volume fraction of amorphous grain boundary region in the films was critical. The first step in determining this was based on a simple cubic system. The same concept was the model for the more complex three dimensional hexagonal shapes that more accurately represent the shapes of real grains.

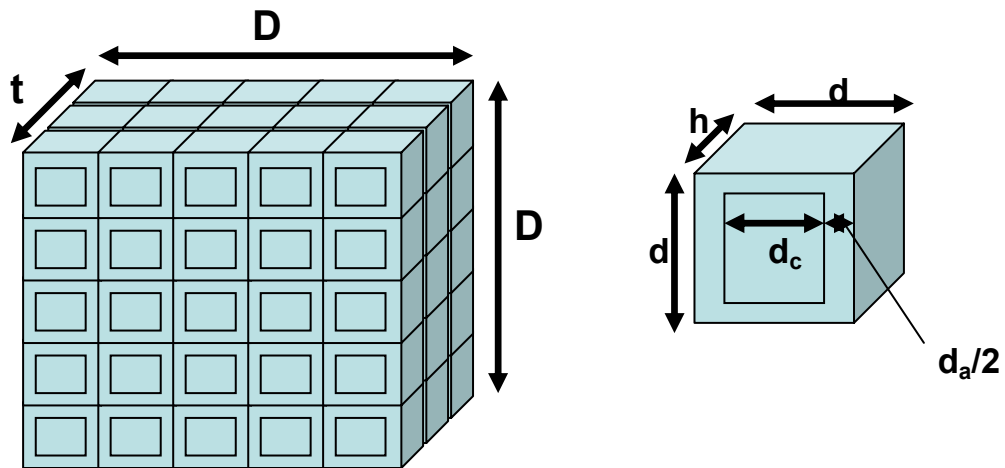


FIGURE 7.1. Cubic system basis for amorphous volume fraction calculations.

$D$  = length and width of total region

$t$  = thickness of total region (film thickness)

$d$  = length and width of grain + grain boundary

$h$  = height of grain + grain boundary

$d_a$  = width of amorphous region

$d_c$  = length and width of crystalline region

$d = d_c + d_a$

Volume of total region =  $D^2t$

Volume of grain + grain boundary =  $d^2h$

Number of grains =  $D^2t / d^2h$

Volume of crystal =  $(d-d_a)^2h$

Volume of amorphous region around each grain = (volume of grain – volume of crystal)  
=  $d_a h (2d - d_a)$

Volume Fraction of Amorphous Region =  $\frac{\text{volume of amorphous region}}{\text{volume of total region}} * (\# \text{ of grains})$

$$= \frac{d_a h (2d - d_a)}{D^2 t} * \frac{D^2 t}{d^2 h}$$

$$= \frac{d_a (2d - d_a)}{d^2}$$

**Volume Fraction of Amorphous Region for Cubic System ( $V_f$ ) =  $\frac{d_a (2d - d_a)}{d^2}$**

### 7.1.2. 3-D Hexagonal System

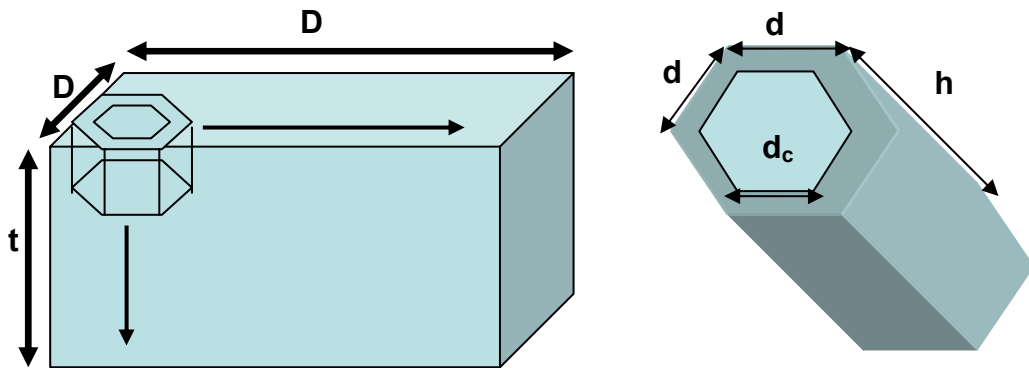


FIGURE 7.2. 3-D hexagonal system for amorphous volume fraction calculations.

$D$  = length and width of total region

$t$  = thickness of total region (film thickness)

$d$  = length and width of grain + grain boundary

$h$  = height of grain + grain boundary

$d_a$  = width of amorphous region

$d_c$  = length and width of crystalline region

$$d = d_c + d_a$$

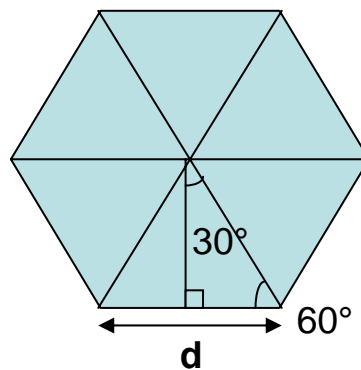


FIGURE 7.3. Hexagon surface for area calculation.

$$\text{Volume of total region} = D^2t$$

$$\text{Volume of grain + grain boundary} = \frac{3\sqrt{3}}{2} d^2h$$

$$\text{Number of grains} = \frac{D^2t}{\frac{3\sqrt{3}}{2} d^2h}$$

$$\text{Volume of crystal} = \frac{3\sqrt{3}}{2} (d-d_a)^2h$$

$$\begin{aligned} \text{Volume of amorphous around each grain} &= (\text{volume of grain} - \text{volume of crystal}) \\ &= \frac{3\sqrt{3}}{2} d_a h (2d-d_a) \end{aligned}$$

$$\text{Volume Fraction of Amorphous Region} = \frac{\text{volume of amorphous region}}{\text{volume of total region}} * (\# \text{ of grains})$$

$$= \frac{\frac{3\sqrt{3}}{2} d_a h (2d-d_a)}{D^2t} * \frac{D^2t}{\frac{3\sqrt{3}}{2} d^2h}$$

$$\text{Volume Fraction of Amorphous Region for Hexagonal System } (V_f) = \frac{d_a(2d-d_a)}{d^2}$$

When comparing the volume fraction equations of the cubic and hexagonal systems, it is clear that the two equations are identical. However, this does not mean that the  $V_f$  of amorphous region for the 3-D hexagonal system is equal to that of the cubic system. For the same grain size, the volume fraction of amorphous region is larger for the 3-D hexagonal system than it is for the cubic system. Consider two spherical grains of the same diameter with a cubic crystal and a hexagonal crystal. Figure 7.4 illustrates that with equal “diameter” grains, the values of ‘d’ in the equation for  $V_f$  are different for

each system. The value of 'd' in the cubic system is smaller than that in the hexagonal system by a factor of  $\sqrt{2}$ .

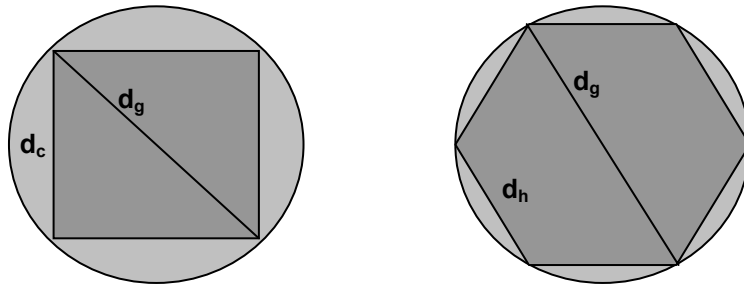


FIGURE 7.4. Equal diameter grains with varying 'd' dimensions between the cubic and hexagonal shapes.

$d_g$  = diameter of grain

$d_c$  = 'd' dimension of cubic system

$d_h$  = 'd' dimension of hexagonal system

$$d_g = \sqrt{2} d_c = 2 d_h$$

Therefore,  $d_c = \sqrt{2} d_h$

To determine  $V_f$  of amorphous region as a function of grain size for the nanocrystalline zirconium films, a known value for  $d_a$  was considered, leaving only  $d$  (grain size) as the variable parameter. An average value of  $d_a$  was used from the basic geometry of a grain boundary with respect to the lattice and the Burger's vector. Figure 7.5 demonstrates this relationship [19].

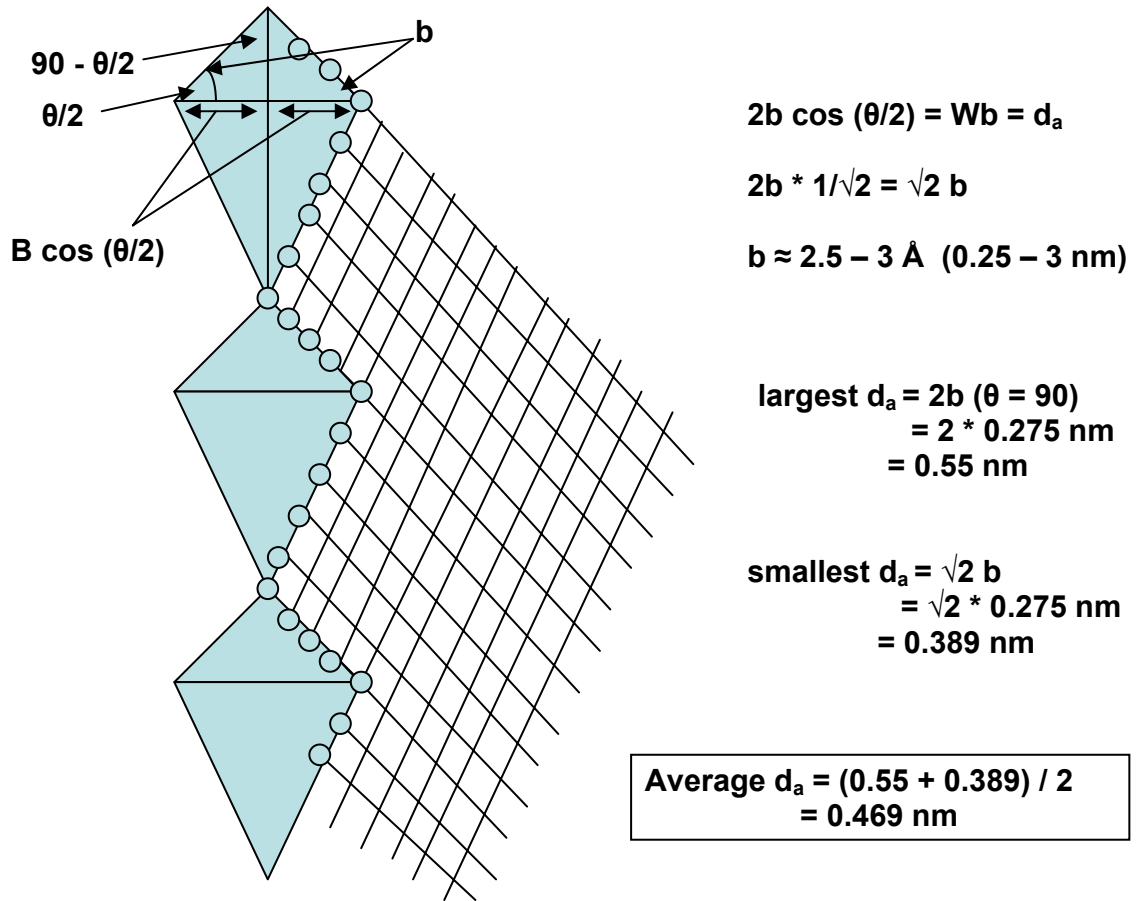


FIGURE 7.5. Illustration for determining the average amorphous region per grain.

Letting the average  $d_a = 0.469 \text{ nm}$ , the equation for volume fraction of amorphous region in the films is:

$$V_f = \frac{0.938 d - 0.219961}{d^2}$$

Using this equation, volume fraction of amorphous grain boundary region was determined for several values of grain size in the nanocrystalline range, as shown in figure 7.6.

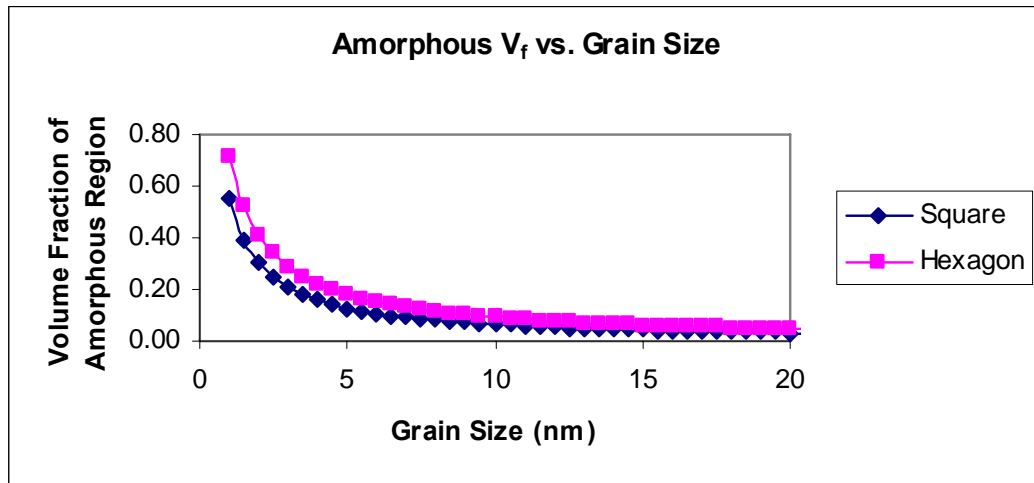


FIGURE 7.6. Graph illustrating the effect of grain size as well as grain shape on the amorphous volume fraction of a system.

It is clear from figure 7.6 that for the same size grain, the hexagonal shape results in a larger volume fraction of amorphous region than does the cubic (“square”) shape. The grains with more complex geometry may be considered by representation with polygons. Grains of these shapes lead to a large volume fraction of amorphous region. It is also evident that the amorphous volume fraction drastically increases at grain sizes less than 5 nm. With this information, it is apparent that the low temperature deposited zirconium films with grain size between 3 and 5 nm contains a much larger volume fraction of amorphous grain boundary region, leading to a significant increase in the amount of hydrogen storage possible, as well as creating a faster path for hydrogen diffusion.

## 8. CONCLUSIONS AND FUTURE WORK

The synthesis of nanocrystalline films of Zr and Ti was successful via low temperature physical vapor deposition. The low temperature films proved to have grains of smaller size than that of the room temperature deposited films. The presence of hydrogen was detected in the films that were subjected to hydrogen treatments of both molecular charging and plasma treatment, and characterization proved a higher concentration of hydrogen in the lower temperature deposited films than in the room temperature deposited films.

From scanning electron microscopy images of sample morphology, the nanocrystalline films of Ti and Zr exhibited rather large surface areas for the absorption of hydrogen due to the very porous nature of the alumina substrate.

X-ray diffraction and high resolution transmission electron microscopy gave results supporting the idea of achieving smaller grain sizes at low temperature depositions as opposed to higher temperature or room temperature depositions. Through X-ray diffraction, smaller grain sizes are noted by peak broadening at various reflections, as well as by crystallite size comparisons calculated from the Scherrer Equation, using full width at half maximum data from the “Jade” software program. High resolution transmission electron microscopy showed that the average grain size of the room temperature deposited films of Ti and Zr was between 15 and 20 nanometers, while the

average grain size of the low temperature deposited films was between 3 and 5 nanometers.

In terms of identification of elements and observation of hydrides, X-ray diffraction gave evidence that the zirconium films were in fact zirconium with characteristic Zr peaks around  $32^\circ$ ,  $34^\circ$ , and  $66^\circ$  (2-Theta degrees), with a notable  $ZrH_{0.25}$  peak around 2-Theta equal to  $34.5^\circ$ . Similarly, this technique proved titanium peaks in the nanocrystalline titanium films with characteristic Ti peaks around 2-Theta equal to  $35^\circ$  and  $38^\circ$ . Optical microscopy illustrated the presence of hydrides in the Zr films, by which the hydrides were then verified using scanning electron microscopy mapping and line scan which gave results that the K-alpha signals of carbon and oxygen were very low with respect to even background noise and extremely low with respect to the silicon and zirconium signals. For further verification of hydrides, resistivity measurements (plots of resistance versus temperature) proved significantly higher resistance levels in the hydrogen treated samples as opposed to those not subjected to hydrogen charging, as well as higher resistance levels in the lower-temperature deposited, hydrogen treated films over the room-temperature deposited, hydrogen treated film. Finally, Secondary ion mass spectrometry depth profiling directly validated the presence of hydrogen in the hydrogen treated films by graphically illustrating  $1 \times 10^7$  counts/sec of hydrogen in the hydrogen treated films as opposed to the approximate  $1.4 \times 10^4$  counts/sec of hydrogen in the non-hydrogen treated films.

From testing of kinetics of various nanocrystalline, hydrogenated and non-hydrogenated films, the results are not discernable due to the extremely low weights of the films, averaging 0.6 mg with corresponding lower weights of hydrogen concentration. With such low weight films, even the known maximum hydrogen capacity of about 7 wt% achieved thus far, would equal to less than 0.05 mg weight in the experimental films, which would be extremely difficult to detect with the method of testing of kinetics that was employed. Fusion analysis is expected to be useful for this purpose.

Analytical modeling in conjunction with experimentally determined grain size range of the nanocrystalline films, it is evident that the amorphous volume fraction drastically increases at grain sizes less than 5 nm, and with the grain size of the low temperature deposited films ranging between 3 and 5 nm, the low temperature deposited zirconium films contain a much larger volume fraction of amorphous grain boundary region, and thus the potential for significantly increased hydrogen storage capability, as well as a much faster path for hydrogen diffusion.

In terms of future work, there are several items to be addressed as mentioned throughout this report. It would be ideal to create nanocrystalline films of Mg alloys, which are well known for their ability to contain large weight percentages of hydrogen. It may also be beneficial to create thicker films with the potential for storing more hydrogen, so that hydrogen weight percent characterization may be more accurate. Along these lines, data on quantitative hydrogen concentration of the films should be done by means of further

SIMS analysis with hydrogen implantation. Testing the kinetics with a Sievert's apparatus is important as kinetics of absorption and desorption are critical aspects for the use of metal hydrides in fuel cells. Also, it would be interesting as well as imperative to determine a cost effective method for production of these metal hydrides in addition to charging techniques in order to incorporate the fuel cell into the lives of the average American.

## 9. BIBLIOGRAPHY

- (1) T. Klassen, W. Oelerich, K. Zeng, and R. Bormann, Nanocrystalline Mg based alloys for hydrogen storage, GKSS-Forschungszentrum Geesthacht GmbH, 1998, p. 11.
- (2) R. Schulz, J. Huot, G. Liang, S. Boily, G. Lalande, M.C. Denis, J. P. Dodelet, Recent Developments in the applications of nanocrystalline materials to hydrogen technologies, *Mat. Sci. Engng.*, 1999, v. 267A, p. 240-245.
- (3) J. Huot, G. Liang, and R. Schulz, Mechanically alloyed metal hydride systems, *Applied Physics* 2001, v. 72A, p. 187-195.
- (4) L. Zaluski, A. Zaluska, P. Tessler, J. O. Stroem , and R. Schulz, Nanocrystalline hydrogen absorbing alloys, *Mater. Sci. Forum*, 1996, v. 225-227, p. 853-858.
- (5) G. Liang, J. Huot, S. Boily, A. Van Neste, and R. Schulz, Catalytic effect of transition metals on hydrogen sorption in nanocrystalline ball milled MgH<sub>2</sub>-Tm (Tm=Ti,V,Mn,Fe, and Ni) systems, *J. Alloys and Compounds*, 1999, v. 292, p. 247-252.
- (6) W. Oelerich, T. Klassen, and R. Bormann, Metal oxides as catalysts for improved hydrogen sorption in nanocrystalline Mg-based materials, *J. Alloys and Compounds*, 2001, v. 315, p. 237-242.
- (7) W. Oelerich, T. Kalsen, and R. Bormann, Mg-based hydrogen storage materials with improved hydrogen sorption, *Mater. Trans.*, 2001, v. 42, p. 1588-1592.
- (8) Pinkerton, Frederick E. and Wicke, Brian G. Bottling the Hydrogen Genie. *The Industrial Physicist*. 2004, 112, 536.

- (9) [www.eere.energy.gov/hydrogenandfuelcells](http://www.eere.energy.gov/hydrogenandfuelcells)
- (10) Birnbaum, H. Fueling the Freedom Car. *Materialstoday*. 2005, *19*, 344.
- (11) Schlapbach, L. Hydrogen as a Fuel and its Storage for Mobility and Transport. *MRS Bulletin*. September 2005.
- (12) Bowman, R.; Fultz, B. Metallic Hydrides I: Hydrogen Storage and Other Gas Phase Applications. *MRS Bulletin*. September 2002.
- (13) J. A. Eastman, L. J. Thompson, and B. J. Kestel, Narrowing of Pd-H miscibility gap in nc-Pd, *Phys. Rev.*, 1993, v. 48B, p. 84-92
- (14) A. Y. Esayed, Hysteresis and thermodynamic characterization of Ni<sub>1-x</sub>Cr<sub>x</sub> (x=0.03,0.05,0.1), *Int. J. Hydrogen Energy*, 2000, v.25, p. 363-368.
- (15) J. H. Woo, C. B. Jung, J. H. Lee, and K. S. Lee, Electrochemical characteristics of nanocrystalline ZrCr<sub>2</sub> and Mg<sub>2</sub>Ni type metal hydrides prepared by mechanical alloying, *J. Alloys and Compounds*, 1999, v. 293-295, p. 556-563.
- (16) L. Maya, W. R. Allen, A. L. Glover, and J. C. Mabon, Gold Nanocomposites, *J. Vac. Sci. Technol.*, 1995, v.13, p. 361-365.
- (17) R. Schulz, G. Lalande, J. Huot, S. Boily, M. C. Denis, S. Bouaricha, D. Guay, and J. P. Dodelet, Porous nanocrystalline alloys prepared by energy ball milling, *Mater. Sci. Forum*, 1998, v. 269-272, p. 1055-1060.
- (18) <http://www.cea.com/tutorial.com>
- (19) Kehl, G. L., *The Principles of Metallographic Laboratory Practice*, 1949, Eurasia Publishing.

(20) Cullity, B. D., Elements of X-ray Diffraction, 1967, Addison-Wesley, p. 99.

(21) Hirth, J.P., Lothe, J. Theory of Dislocations, 1992, Krieger Publishing Company, p. 515.

(22) <http://hyperphysics>

(23) [www.gkss.de](http://www.gkss.de)